Research Square

Preprints are preliminary reports that have not undergone peer review.
They should not be considered conclusive, used to inform clinical practice,
or referenced by the media as validated information.

Attribution of Anthropogenic Impact on Extreme Mei-yu Rainfall in Taiwan

Chung-Chieh Wang
National Taiwan Normal University
Fang-Yu Su
National Taiwan Normal University
Kai-En Chuang
National Taiwan Normal University
Li-Shan Tseng
sian@ntnu.edu.tw

National Taiwan Normal University

Article

Keywords:

Posted Date: November 10th, 2026

DOI: https://doi.org/10.21203/rs.3.rs-11461417/v1

License: This work is licensed under a Creative Commons Attribution 4.0 International License.
Read Full License

Additional Declarations: No competing interests reported.

Attribution of Anthropogenic Impact on Extreme Mei-yu Rainfall in Taiwan

Chung-Chieh Wang, Fang-Yu Su, Kai-En Chuang, Li-Shan Tseng*

Department of Earth Sciences, National Taiwan Normal University, Taipei, Taiwan.

*Corresponding author. Email: sian@ntnu.edu.tw

Abstract

Mei-yu rainfall provides vital water resources to Taiwan, but this quasi-stationary system has produced increasingly severe flooding in recent decades. We investigate the influence of anthropogenic climate change on two extreme Mei-yu events (11–12 June 2012 and 2–3 June 2017) using a pseudo-global-warming (PGW) approach, forcing the Cloud-Resolving Storm Simulator (CReSS) model with anthropogenic climate change signals derived from differences between 15 CMIP6 historical and natural simulations over May–June 2000–2014. Five sensitivity experiments per event, each initialized from a different analysis and reanalysis product (ERA5, CFSv2, FNL, MERRA-2, JRA-55), test the variability of the results. We find that anthropogenic forcing drives two competing effects: increased moisture enhances frontal rainfall, while a weakened southwesterly flow suppresses it. The balance between these effects depends on the synoptic setting, making simulated changes in Mei-yu frontal precipitation under warming somewhat case-dependent. In the 2012 event (moderate front, strong flow), enhanced moisture dominated and led to increased rainfall over Taiwan. In the 2017 event (intense front, moderate flow), the simulated frontal position instead controlled the outcome, with an offshore shift reducing rainfall over Taiwan. These contrasting outcomes suggest that projecting future Mei-yu rainfall risk requires not only accounting for mean-state warming but also considering event-specific synoptic controls—complicating flood-risk assessments for Taiwan.

Introduction

Anthropogenic greenhouse gas and aerosol emissions are now the dominant driver of observed warming[1], with documented impacts on the East Asian summer monsoon (EASM), including intensified extreme rainfall despite a decline in total seasonal precipitation[2]. Located within the East Asian monsoon region, Taiwan experiences its Mei-yu season from May to June[3]. During this period, repeated frontal passages become quasi-stationary as continental cold air weakens and the subtropical high strengthens, producing prolonged rainfall[4,5]. Heavy rainfall often develops when the prefrontal southwesterly flow intensifies into a low-level jet (LLJ)[6,7]. With abundant moisture, the LLJ combines with local convergence and Taiwan's steep topography to trigger intense mesoscale convective systems (MCSs), which are the dominant source of Mei-yu precipitation[8,9]. Taiwan's complex terrain shapes precipitation through orographic lifting[10] and flow deflection and blocking[11], thereby modulating the spatial distribution of Mei-yu rainfall.

Amid ongoing climate change, the Mei-yu system has shifted away from its traditionally persistent, gentle-rain character, trending toward more frequent extreme rainfall events[12], reduced frequency of light precipitation and enhanced spatial heterogeneity[13], and longer dry spells[14]. This pattern aligns with the anthropogenic disruption of monsoon staging across East Asia more broadly[15], yet the anthropogenic contribution to individual extreme Mei-yu rainfall events remains poorly constrained. Recent record-breaking events, such as the 2020 Yangtze River flooding—the worst since 1961[16,17]—underscore the urgency of quantifying anthropogenic contributions to extreme Mei-yu rainfall.

Extreme event attribution has made significant progress in recent years[18,19,20,21]. While traditional approaches rely on large ensembles of global climate model simulations[22,23], the pseudo-global-warming (PGW)[24,25,26,27,28] approach has emerged as a strong alternative for regional extreme events: by imposing climate change signals on the initial and boundary conditions while preserving the observed synoptic evolution, PGW enables process-level study of how anthropogenic warming affects specific meteorological systems[29] and is particularly well suited to terrain-influenced rainfall that coarse global models struggle to resolve[30,31].

Most attribution studies of extreme rainfall near Taiwan have focused on typhoons, given their substantial contribution to hydrometeorological disasters and the easier generalization of results

to tropical cyclones around the globe[32,33]. The Mei-yu frontal system remains comparatively understudied because of its multiscale interactions, the shorter lifespans of its MCSs, and the complexity of the terrain. Prior analyses have generally relied on coarse-resolution CMIP5/6 global models[34,35], which have known limitations in resolving the small-scale monsoon rainbands and local physical processes needed to capture extreme precipitation events. Consequently, how anthropogenic forcing alters the structure and dynamics of the Mei-yu front itself and the associated MCSs—rather than just its broader seasonal rainfall totals—remains poorly understood.

In this study, we examine two representative extreme Mei-yu events in northern Taiwan, both exceeding the Central Weather Administration (CWA) threshold for extremely heavy rainfall (≥500 mm/24 h): 11–12 June 2012, characterized by a moderate front embedded in strong southwesterly monsoon flow with a well-developed LLJ[36,37,38], and 2–3 June 2017, marked by an intense front with moderate southwesterly flow and strong orographic enhancement[39,40]. Together, these cases span the range of frontal-flow configurations observed during Taiwan's Mei-yu season, providing a useful framework for examining how anthropogenic forcing affects different modes of extreme rainfall. Using the PGW approach and the Cloud-Resolving Storm Simulator (CReSS), we quantify anthropogenic contributions by comparing present-day and counterfactual natural-climate experiments, and employ additional atmospheric datasets to assess the variability and robustness of the identified anthropogenic impacts.

Results

Overview of the two extreme Mei-yu events

The 2012 event began on 10 June, when enhanced southwesterly flow triggered widespread convection over southern Taiwan via orographic lifting, with reflectivity reaching 45–55 dBZ (Figs. 1a–c; Fig. 2c and point 1 in Fig. 2a). As the front moved southward, a quasi-linear, intense rainband formed over northern Taiwan and remained nearly stationary for approximately 10 h (Figs. 1d–f; Figs. 2d–e and point 2 in Fig. 2a). Peak rainfall occurred as the front interacted with the southwesterly flow, producing the maximum precipitation recorded across Taiwan during the

event (Figs. 1f–g; Fig. 2e and point 3 in Fig. 2a). The system then moved into southern Taiwan, where frontal activity and moisture transport declined, weakening the event (Figs. 1h–i; Fig. 2f and point 4 in Fig. 2a). Three-day rainfall totals over 10–12 June in the southern mountains exceeded 1500 mm driven primarily by the LLJ[41] (Figs. 2c–e), while northern Taiwan recorded historic daily rainfall totals during the early hours of 12 June (Figs. 2a, e).

The 2017 event exhibited a contrasting temporal pattern. The front and rainband reached northern Taiwan on the evening of 1 June and remained quasi-stationary on the morning of 2 June, producing short bursts of extreme rainfall along the northern coast (Figs. 3a–c; Figs. 4b–c and point 1 in Fig. 4a). Then, the front and rainband moved southward (Figs. 3d–f; Fig. 4d and point 2 in Fig. 4a). On 3 June, the front briefly shifted northward and the MCSs expanded, leading to substantial rainfall across Taiwan (Figs. 3g–h; Fig. 4d and point 3 in Fig. 4a), then the event gradually weakened (Fig. 3i; Fig. 4e). The high accumulated rainfall underscores the event's extreme nature. In northern Taiwan, hourly rainfall exceeded 80 mm at several rain gauge stations, with a peak daily rainfall of 772 mm at Sanzhi (Fig. 4c). Similarly, the central and southern mountains experienced extreme precipitation, with total rainfall reaching 975 mm (Figs. 4c–d).

Main features of the Anthropogenic climate change signal

The signals of anthropogenic climate change in the modern era as computed from the ensemble of CMIP6 model simulations are presented in Fig. 5. At low levels (850 hPa), the western North Pacific subtropical high intensifies and extends westward, forming an anomalous anticyclonic circulation southwest of Taiwan (Fig. 5a). Northeasterly winds (0.4–1.0 m s^{-1}) flow off the southern flank of the anticyclone over the South China Sea, yielding a weakened southwesterly summer monsoon. As a result, the weakened LLJ curtails the transport of warm, moist air from the South China Sea, a vital source of Mei-yu precipitation[7]. This also reduces frontal lifting and orographic forcing, both essential for driving heavy rain events over Taiwan. These findings align with previous research linking higher aerosol concentrations to preferential continental cooling and a reduced land–sea thermal contrast[34]. Such effects contribute to a weakened EASM, although our study considers a combined anthropogenic signal without separating the specific contributions of aerosols and greenhouse gases. At mid-levels (500 hPa), the changes are

relatively minor (around 5% of climatology; Fig. 5b): a geopotential height center (21.5–22 m) forms southeast of Japan, with easterly winds (0.3–0.6 m s^{-1}) to its south, further weakening the climatological westerlies. At upper levels (200 hPa), anthropogenic warming enhances the subtropical westerly jet, increasing wind speeds by 1.0–1.4 m s^{-1} (Fig. 5c). In contrast, divergence at upper levels over Taiwan is significantly reduced, decreasing dynamical support for low-level convergence and making conditions less favorable for deep convection. Overall, this juxtaposition of strengthened westerlies but weakened divergence indicates less favorable conditions for Mei-yu frontal convection.

Beyond these dynamic changes, anthropogenic forcing also drives distinct shifts in the thermodynamic fields relevant to Mei-yu rainfall. At low levels, a northeast–southwest warming band (0.8–1.0 K) spans Taiwan, aligning with the Mei-yu front (Fig. 5d). However, the warming difference between upper and lower levels reduces the tropospheric lapse rate, increasing static stability and suppressing deep convection (Fig. 5e). Meanwhile, specific humidity increases throughout the troposphere, following the Clausius–Clapeyron relationship, which dictates approximately a 7% rise in saturation vapor pressure per 1 K of warming[42] (Fig. 5f). Notably, the moisture increase over the corridor from southwest Taiwan to the South China Sea (0.1–0.3 g kg^{-1}) is smaller than in the surrounding environment, reflecting the weakened southwesterly flow and reduced moisture advection (Fig. 5d).

Taken together, these dynamic and thermodynamic changes act in partially opposing directions: increased moisture and a strengthened upper-level westerly jet favor more intense precipitation, whereas enhanced static stability, weakened low-level moisture transport, and reduced upper-level divergence inhibit convective development. This competition between reinforcing and suppressing factors makes it difficult to determine the net anthropogenic influence on Mei-yu rainfall from large-scale diagnostics alone. We therefore use the CReSS model, together with water budget analysis, to identify the specific physical processes that drive the simulated rainfall response to anthropogenic forcing.

Anthropogenic impact on frontal intensity and movement

Comparing observations with five CEs in the 2012 case shows that the CReSS model effectively captures the strengthening and southward movement of Mei-yu fronts over Taiwan (Figs. 6a and

6b). Among the five CEs, CFSv2_CE (Fig. 6b, 1st column) most closely matches observed frontal positions and moving speeds. Notably, JRA-55_CE (Fig. 6b, 4th column) failed to capture the front over northern Taiwan (~25°N) but anomalously simulated a rainband over southern Taiwan. This southward shift is suspected to reflect JRA-55's known boundary uncertainties. Specifically, its climatological warm-season wet bias south of 25°N[43] and dry bias along the 20°–30°N band[44] suggest a less favorable background environment for northern convergence. Furthermore, we cannot rule out the possibility that a documented negative bias in JRA-55's low-level nocturnal meridional winds[45] might have restricted northward monsoonal moisture transport, suppressing frontal development over northern Taiwan. Conversely, MERRA-2_CE (Fig. 6b, 5th column) fails to capture a coherent frontal structure, likely due to notable systematic dry biases and underestimation of flood-season rainfall and heavy precipitation, characteristics of MERRA-2 in this region[46].

Comparing CE to SE, particularly for CFSv2, ERA5, and FNL (Fig. 6b and 6c, 1st–3rd columns), shows that anthropogenic forcing delays the front's approach to Taiwan by 1–4 hours and amplifies and concentrates the frontal structure as it passes over Taiwan on 12 June. This is consistent with the competing dynamic and thermodynamic effects described above, in which the strengthened frontal structure suggests the thermodynamic response outweighs the dynamic deficit in these experiments. In contrast, the JRA-55 simulation shows a clearer frontal structure over northern Taiwan in SE than in CE (Fig. 6c vs. 6b, 4th column)—the opposite response—potentially reflecting JRA-55's greater uncertainty in resolving boundary layer processes under statically unstable conditions, though this would require further targeted investigation to confirm.

In the 2017 case, compared with observations (Fig. 6d and 6e), the four experiments other than MERRA-2 successfully reproduce the front's southward evolution over Taiwan (Fig. 6f). CFSv2, ERA5, and FNL (Fig. 6f, 1st–3rd columns) align most closely, whereas JRA-55 (Fig. 6f, 4th column) shows somewhat excessive frontal progression speed, and MERRA-2 (Fig. 6f, 5th column) again fails to reproduce a coherent frontal structure. The SEs (Fig. 6g) show notable differences among simulations: in CFSv2, the front is clearly weaker in CE than in SE, whereas in ERA5, FNL, and JRA-55, differences in frontal strength between CE and SE are less pronounced. In CFSv2, ERA5, and FNL, frontal signals south of Taiwan are weaker in CE than in SE, consistent with the anthropogenic weakening of southwesterly moisture transport discussed above.

The frontal center track analysis (Fig. 7) further demonstrates that the response to anthropogenic forcing varies by case. In 2012 (Fig. 7a and 7b), the response shows clear phases over time: on 12 June (red line), anthropogenic forcing significantly enhances the signal over the offshore area east of Taiwan, shifting the frontal center eastward/northward in ERA5, FNL, and JRA-55; by 13 June (blue line), it consistently drives a northward movement toward Taiwan, except in MERRA-2. In contrast, the 2017 event exhibits greater uncertainty (Fig. 7c and 7d): anthropogenic forcing generally moves the tracks offshore on 2 June (red line). In CFSv2, a stronger eastern frontal signal causes the frontal center to oscillate between Taiwan's eastern and western sides, producing a less clearly defined frontal position, whereas ERA5 and FNL shift westward. On 3 June (blue line), responses diverge further: CFSv2 and FNL shift northward, whereas ERA5 shifts southward. This irregularity may reflect heightened sensitivity to small initial-condition differences under weak dynamical forcing, likely compounded by differences in model physics and parameterization across the reanalysis products.

Anthropogenic impact on precipitation

CReSS reasonably reproduces Mei-yu convective structures across the five experiments, as indicated by the vertical maximum mixing ratios of precipitation hydrometeors, including rain (q_r), graupel (q_g), and snow (q_s) (q3max; Fig. 8). CFSv2_CE provides the closest match to observations. ERA5_CE and FNL_CE simulate broader but weaker convection. JRA-55_CE displays overly concentrated and intense systems, and MERRA-2_CE shows the most diffuse structures. Anthropogenic forcing affects convective structure differently across these experiments: ERA5, FNL, and MERRA-2 show minimal sensitivity between CE and SE; JRA-55 consistently shows more concentrated and intense convection under anthropogenic forcing; and CFSv2 shows a nonlinear response—little change in 2012 and more dispersed convection in 2017.

Changes in accumulated precipitation ($CE - SE$) reveal significant regional effects of anthropogenic forcing that vary through the 2012 event (Fig. 9a and 9b). During the first two days (10–11 June, Fig. 9a), driven primarily by the southwest monsoon with topographic effect (Fig. 2a, point 1), precipitation decreases by roughly 200–300 mm across southern Taiwan in all experiments except MERRA-2 (Fig. 9a, 5th column). This decline indicates that, during this

phase, anthropogenic weakening of the southwest monsoon and the associated reduction in moisture transport dominate the precipitation response. During the last two days (12–13 June, Fig. 9b), when both the southwest monsoon and the frontal system contribute to rainfall (Fig. 2a, points 2–4), the response reverses: precipitation increases by roughly 200–250 mm across southern Taiwan in all five experiments, with JRA-55 showing a localized increase of about 600 mm over the southernmost part of the island (Fig. 9b, 4th column). This reversal is consistent with the competing dynamic and thermodynamic effects described above: once the front is established, the thermodynamic response—increased atmospheric moisture and saturation vapor pressure—outweighs the dynamic weakening of the southwesterly flow, intensifying precipitation over much of southwestern Taiwan.

In the 2017 case (Fig. 9c and 9d), the anthropogenic precipitation response diverges from one phase to the next. During the first phase (2000 LST 1 June – 1200 LST 3 June, Fig. 9c), when the front reaches northern Taiwan and moves southward (Fig. 4a, points 1–2), rainfall decreases more often than increases across Taiwan—particularly along the north coast, central mountains, and south coast—in all experiments except JRA-55 (Fig. 9c, 4th column). During the second phase (1200 LST 3 June – 0000 LST 5 June, Fig. 9d), when the front moves northward again and brings rainfall to northern, central, and southern Taiwan (Fig. 4a, point 3), the response becomes strongly dependent on shifts in the frontal track (Fig. 7c and 7d, blue line). In CFSv2 (Fig. 9d, 1st column), anthropogenic forcing shifts the frontal center toward Taiwan, sharply increasing island-wide rainfall. ERA5 and FNL (Fig. 9d, 2nd–3rd column) show the opposite behavior: under anthropogenic forcing, their frontal centers shift away from Taiwan, driving a significant decrease in rainfall. JRA-55 (Fig. 9d, 4th column) instead shows a substantial increase in southern Taiwan once again, on the order of 300–350 mm, while MERRA-2 (Fig. 9d, 5th column) shows increased rainfall concentrated in central Taiwan. Unlike 2012, when a consistent shift between dynamic and thermodynamic dominance governed the anthropogenic response, the 2017 response is driven primarily by anthropogenic shifts in the frontal track, which vary in direction and magnitude across the five experiment pairs.

Precipitation intensity–frequency analysis (Fig. 10) shows that all experiments except CFSv2 exhibit precipitation extremization—more heavy precipitation and less light precipitation—consistent with the robust thermodynamic response expected under global warming[47]. CFSv2

uniquely shows decreased frequency across all intensity bins, suggesting that dynamic suppression offsets the thermodynamic response in its experiment. This divergent behavior, particularly the reduced frequency of heavy rain, is consistent with CFSv2's documented tendency to underestimate extreme precipitation over East China, widely attributed to the limitations of its Simplified Arakawa–Schubert (SAS) convection scheme[48]. Furthermore, such systematic underestimation of high-intensity rainfall by CFSv2 is a known, robust model deficiency also reported in other monsoon regions, such as South Asia, where it consistently struggles to capture extreme precipitation events compared with other reanalysis products, such as ERA5[49].

Water budget analysis

Water budget results are presented separately for the Taiwan domain and the dynamic frontal domain, for both the 2012 (Table 3–Table 5) and 2017 (Table 6–Table 7) cases.

In the 2012 case, the Taiwan-domain anthropogenic response differs markedly between the event's two phases (Fig. 9): a consistent decrease in precipitation during the monsoon-dominated first phase, and a dataset-dependent response during the combined front-and-monsoon second phase. Phase 1 (10–11 June). Across the Taiwan domain (Table 3), mean rainfall (P) is dominated by CVF (72–86%) at the lateral boundaries in all four experiments; the remaining terms (TDC, CHF, E, R) are one to two orders of magnitude smaller and together account for only 10–30% of P. All four experiments show a consistent anthropogenic response during this phase: P decreases under anthropogenic forcing, driven by a weakening of CVF. In each experiment, CVF is dominated by ADV, reflecting a significant reduction in low-level moisture transport (or increase in dry inflow) that outweighs the CONV contribution. Notably, anthropogenic forcing increases CONV in three of the four experiments (all except CFSv2), but this increase is insufficient to offset the negative ADV effects, and overall CVF weakens.

Phase 2 (12–13 June). Averaged over the Taiwan domain (Table 4), the anthropogenic response varies across experiments. CFSv2 and JRA-55 show a slight increase in P: in CFSv2, driven mainly by a modest strengthening of CHF; in JRA-55, by a strengthening of CVF, itself driven jointly by increased CONV and increased (moist) ADV. ERA5 and FNL show a slight decrease

in *P*: in ERA5, driven mainly by weakened CVF; in FNL, mainly by weakened TDC, with CONV and ADV within CVF roughly offsetting one another, leaving only a small net CVF contribution. This decrease is clearly linked to an outward shift of the frontal center in both ERA5 and FNL (Fig. 7). Although anthropogenic forcing intensifies the front overall during this phase, as noted above, it also displaces the front outward in these two experiments. The front moves away from Taiwan even as it strengthens, therefore producing a net decrease in rainfall over the island domain (Fig. 2b).

In the dynamic frontal domain (Table 5), all four experiments consistently show increased *P*, driven primarily by enhanced CVF, which is itself dominated by strengthened CONV; the weakening of CHF partially offsets this increase. ERA5 shows a more pronounced moderating effect from *R*.

In the 2017 case over the Taiwan domain (Table 6), anthropogenic forcing produces differing precipitation responses across experiments, consistent with the frontal-track shifts identified earlier (Fig. 7). In CFSv2, anthropogenic forcing shifts the front offshore, producing divergent convection and a significant decrease in *P*. ERA5 and FNL show a similar offshore shift and corresponding decrease in *P*, though here convection itself strengthens (positive CONV) while being outweighed by stronger dry ADV. Only in JRA-55, where anthropogenic forcing concentrates the frontal track onshore, does *P* increase, driven by enhanced CONV that outweighs the opposing dry ADV.

In the dynamic frontal domain (Table 7), results again split into two groups: CFSv2 and ERA5 show decreased frontal precipitation, whereas FNL and JRA-55 show increased frontal precipitation. In CFSv2, this decrease is consistent with the frontal-intensity weakening identified earlier (Fig. 6)—the only experiment in which anthropogenic forcing produced a clear, unambiguous weakening of frontal intensity—and is reflected here in decreased CONV. In ERA5, by contrast, frontal intensity showed no clear anthropogenic signal in the earlier analysis, yet the water budget shows dry ADV outweighing positive CONV, with CHF further damping convection; this suggests the precipitation decrease in ERA5 arises from changes in moisture transport rather than a systematic weakening of the front itself. FNL and JRA-55 show increased *P* driven by stronger CONV that counters dry ADV, with JRA-55 also offsetting negative CHF.

Given that only CFSv2 showed a clear frontal-intensity response to anthropogenic forcing, these results indicate that the CONV–ADV balance, rather than frontal intensity alone, is the primary source of anthropogenic uncertainty in 2017 frontal precipitation.

Discussion

This study demonstrates that anthropogenic forcing exerts a clear but far from uniform influence on extreme Mei-yu rainfall over Taiwan, acting through two competing pathways: a thermodynamic pathway, in which increased atmospheric moisture and saturation vapor pressure enhance frontal precipitation, and a dynamic pathway, in which a weakened southwesterly monsoon and an altered frontal position suppress it. Which pathway prevails depends on the synoptic setting of each event and, even within a single event, on its evolving phase. In the 2012 case, where the front was comparatively weak and embedded in a strong monsoon flow, the thermodynamic response dominated once the front was established, producing a net increase in precipitation despite a weakened monsoon—though our water budget analysis reveals that this outcome unfolds in two distinct stages, with an initial monsoon-driven decrease giving way to a front-driven increase as dry advection is overtaken by strengthened convergence and moisture supply. In the 2017 case, where the front was more intense but the monsoon flow weaker, the precipitation response hinged instead on anthropogenic shifts in the frontal track itself: experiments in which the front shifted onshore showed increased rainfall, and those in which it shifted offshore showed decreased rainfall. In other words, the highly nonlinear frontal evolution dictates the rainfall changes in Taiwan.

This contrast points to a broader pattern: events occurring under strong, well-organized monsoon regimes—with a robust LLJ, deep moisture layer, and sustained southwesterly flow, as in 2012—appear to yield more consistent, reliable anthropogenic attribution signals across experiments because the thermodynamic pathway dominates relatively uniformly. By contrast, events developing under more marginal or transitional synoptic conditions, as in 2017, are considerably more sensitive to small differences between analyses and reanalyses because weak dynamical forcing allows initial-condition differences and dataset-specific biases to be amplified

into divergent frontal tracks and precipitation outcomes. This case-specific reliability has a practical implication for future Mei-yu attribution work: robust attribution may be most achievable for strongly forced events, while marginal events—arguably the ones most relevant to understanding shifts in event frequency and location—may require substantially larger reanalysis and/or model ensembles to verify the results.

This case dependence helps reconcile the mixed conclusions in the broader literature on attribution of the Mei-yu and EASM. Prior work has reported that anthropogenic forcing weakens EASM circulation and disrupts its intraseasonal staging[15], while simultaneously intensifying EASM precipitation extremes[2,15]. Our results suggest that this apparent tension is not a contradiction to be resolved with a single sign, but reflects genuinely competing physical mechanisms whose net outcome is event-specific. This is broadly consistent with recent evidence that the misty, persistent character of the traditional Mei-yu–Baiu system has substantially receded under anthropogenic warming[12], replaced by more polarized outcomes; our process-level attribution offers one physical explanation for why that polarization, rather than a uniform intensification, emerges from the underlying dynamics.

Our precipitation intensity–frequency analysis reinforces this picture. Most experiments show the classic "extremization" signature expected under warming—more heavy rainfall and less light rainfall[47]—but CFSv2 uniquely shows decreases across all intensity bins, indicating that dynamic suppression fully offsets the thermodynamic gain in this reanalysis. This divergence is consistent with CFSv2's documented tendency to underestimate extreme precipitation relative to observations, reported independently in both East China and Pakistan[48,49], and illustrates a broader methodological point: because our attribution signal is built on regional simulations forced by five different datasets, the fidelity of each dataset's representation of extremes constrains how much confidence can be placed in any single member's anthropogenic signal.

However, several limitations temper the conclusions above. First, our PGW approach applies a time-mean anthropogenic signal to individual historical events, assuming that large-scale circulation changes can be linearly superimposed on the observed state of the atmosphere. This enables process-level investigation but may not capture nonlinear interactions or thresholds that

could emerge under transient warming. Large-ensemble or multi-decadal simulation approaches could complement our findings by more comprehensively sampling natural variability. Second, our attribution is based on two case studies of extreme events; while these were deliberately selected to span contrasting frontal-flow configurations, they cannot capture the full range of Mei-yu synoptic variability. While rare by default, additional cases, particularly those representing intermediate or transitional conditions, would strengthen the conclusions about the reliability of regime-dependent attribution. Third, our five-member reanalysis ensemble, while larger than many single-reanalysis attribution studies, remains limited in size; two datasets (JRA-55 and MERRA-2) showed known systematic biases that degraded their ability to reproduce observed frontal structure. Fourth, because ΔANT combines greenhouse gas and aerosol forcing without decomposition, we cannot separate their individual contributions to the observed dynamic weakening, even though prior work implicates aerosol-driven changes in land–sea thermal contrast as a plausible contributor[34]. Finally, our use of a single regional model (CReSS) means that structural and parameterization uncertainties in convective and microphysical processes are not sampled, which could shift the balance between the dynamic and thermodynamic pathways identified here.

These findings have practical implications for flood-risk assessment in Taiwan and, more broadly, for regions where frontal precipitation systems intersect with monsoon flows. Because the sign and magnitude of the anthropogenic precipitation response depend on event-specific synoptic controls—and on how reliably those controls can be attributed—flood-risk projections based on aggregated climatological trends risk understating the full range of plausible outcomes for individual extreme events. A systematic classification of Mei-yu events by synoptic regime, followed by targeted attribution studies across a broader ensemble of models and datasets, would help clarify which event types can be confidently attributed and which remain subject to irreducible dynamical uncertainty. As global warming continues, understanding which synoptic settings favor thermodynamic dominance versus dynamic and track-driven suppression will be essential for anticipating how Taiwan's Mei-yu flood risk—and that of similar frontal-monsoon systems elsewhere in East Asia—evolves in a warming climate.

Methods

Estimating anthropogenic climate change

Anthropogenic climate change (ΔANT) is derived from the Coupled Model Intercomparison Project Phase 6 (CMIP6)[50] and its subproject, the Detection and Attribution Model Intercomparison Project (DAMIP)[51]. CMIP6 historical simulations include all major anthropogenic and natural forcings, whereas DAMIP provides historical simulations driven by individual forcings or subsets—including natural-only (hist-nat), greenhouse-gas-only (hist-GHG), and aerosols-only (hist-aer)—to isolate their contributions. In this study, ΔANT is defined as the difference between the historical and hist-nat simulations:

$$\Delta ANT = \langle \text{Historical} - \text{hist-nat} \rangle_{2000–2014}$$

where ⟨ ⟩ denotes the ensemble mean, comprising 15 CMIP6 models (Table 1) selected from 134 available models based on the availability of both historical and hist-nat simulations with monthly data for 2000–2014. The ensemble mean spans 19 pressure levels (1000–1 hPa) and includes geopotential height (z), temperature (T), zonal and meridional wind components (u, v), specific humidity (q), and surface temperature (T_s). The 2000–2014 period is chosen because anthropogenic warming has accelerated significantly in recent decades[52]. Although traditional climatological averages span 30 years[53], time averaging (such as the 20-year mean[32]) effectively reduces decadal variability while preserving a stronger, more recent anthropogenic signal. Only the May–June average is used to calculate ΔANT, focusing on the anthropogenic climate change most relevant to the two Taiwan Mei-yu events examined in this study.

Data sources

Initial and boundary conditions (IC/BCs) for the model are derived from five global reanalysis and analysis datasets—ERA5, CFSv2, FNL, JRA-55, and MERRA-2 (Table 2)—to evaluate the robustness of simulated anthropogenic impacts on extreme Mei-yu rainfall across different IC/BCs.

Observational data

Model simulations are validated against observational data from multiple sources. Precipitation is obtained from the Quantitative Precipitation Estimation and Segregation Using Multiple Sensors (QPESUMS)[54], which integrates satellite, radar, and rain-gauge observations to provide

high-resolution (0.0125° × 0.0125°, 10-min) gridded precipitation over both oceanic regions and complex terrain. We examine large-scale circulation patterns and synoptic-scale frontal positions using CWA surface weather maps (6-h), while assessing mesoscale convective evolution using CWA composite vertical maximum indicator (VMI) radar reflectivity (1-h). Because CWA surface weather maps are pre-drawn products without an accompanying quantitative plotting methodology, we additionally obtain 3-km, 30-minute gridded wind and convergence fields from the National Science and Technology Center for Disaster Reduction (NCDR) to construct our own frontal environment maps using the same analytical methodology applied to the model output, enabling direct, like-for-like comparison of frontal intensity and structural detail between observations and simulations—a level of quantitative comparison that the pre-drawn CWA maps do not support. These NCDR fields are produced via 3DVar assimilation of Taiwan's dual-polarization radar data (radial velocity and rainwater mixing ratio) into an ERA5-based WRF background, cycled three times at 30-min intervals following a 1-h spin-up.

Numerical experiments

This study uses the Cloud-Resolving Storm Simulator (CReSS)[55,56], version 3.4.2 from Nagoya University, Japan, for high-resolution numerical experiments. The model runs on a 3 km grid with dimensions 1152 × 672 × 52, with the top at 26 km. This configuration covers 3456 km × 2016 km, roughly spanning 105°–140°E and 15°–35°N for both simulated cases (Fig. 11). The vertical grid is stretched, with increasing layer thicknesses, and has an average spacing (Δz) of about 500 m. Time integration uses a split-explicit scheme with time steps of 3 s for slow modes and 1.5 s for fast modes. The physical options are similar to those used in previous studies[57]. Following the PGW method, two sets of experiments are performed for the 2012 case (9–13 June, 5 days) and the 2017 case (30 May–4 June, 6 days), respectively: (1) Control Experiments (CEs), which use the original five IC/BCs to reproduce the Mei-yu front cases; and (2) Sensitivity Experiments (SEs), in which the long-term ΔANT is subtracted from the IC/BCs for all major variables—including temperature, humidity, winds at the surface and all pressure levels, and SST, etc. (excluding topography).

$$\mathrm{SE}_{\mathrm{ICBC}} = \mathrm{CE}_{\mathrm{ICBC}} - \Delta\mathrm{ANT}$$

Since both CEs and SEs use identical model configurations, the differences between the two sets of simulation results ($CE - SE$) can be regarded as the effects of long-term anthropogenic climate change.

In the following section, we present the simulation results for CEs and SEs. Based on the water budget equation[32], we further conduct diagnostic analyses, examine cloud microphysics and moisture-variation processes, quantify the percentage contributions to precipitation differences, and investigate adjustments in atmospheric circulation under anthropogenic influence and their effects on persistent precipitation systems.

Frontal position and dynamic frontal domain

Frontal position is identified using horizontal wind, equivalent potential temperature (θ_e), and relative vorticity (ζ) at 320 m (~1000 hPa). θ_e is derived from potential temperature, pressure, and water vapor mixing ratio following standard thermodynamic relations[58], and its horizontal gradient ($\nabla\theta_e$) is computed as a centered finite difference converted to physical units (K km^{-1}) using the local grid spacing. A grid point is classified as part of the frontal zone where $|\nabla\theta_e|$ exceeds 1×10^{-2} K m^{-1}, ζ exceeds 1×10^{-4} s^{-1}, and horizontal convergence exceeds 1×10^{-4} s^{-1}. The frontal-center position is then determined using a gradient-weighted iterative centroid method. Each frontal-zone grid point is assigned a weight w equal to the square of its θ_e gradient magnitude (i.e., the front mask multiplied by the gradient itself), so that grid points with the strongest gradients contribute most to the center estimate:

$$lon_c = \frac{\sum_i w_i\, lon_i}{\sum_i w_i},\ lat_c = \frac{\sum_i w_i\, lat_i}{\sum_i w_i} \tag{1}$$

where (lon_i, lat_i) are the coordinates of frontal-zone grid points within the analysis domain (117°–125°E, 20°–28°N). If no grid points satisfy the frontal-zone criteria at a given time, the frontal center from the previous time step is retained to avoid division by zero. The estimate is then refined iteratively: at each of three successive iterations, only grid points within 1.5° of the current center estimate are retained (using a great-circle-distance mask), and Equation (1) is recomputed using this restricted subset. This progressively focuses the center estimate on the strongest, most spatially coherent core of the frontal zone. At each iteration, the updated center is validated to lie within the analysis domain; if not, the previous valid center is retained.

$$var_{lon} = \frac{\sum_i w_i\,(lon_i - lon_c)^2}{\sum_i w_i},\ var_{lat} = \frac{\sum_i w_i\,(lat_i - lat_c)^2}{\sum_i w_i},$$
$$\text{conv} = \frac{\sum_i w_i\,(lon_i - lon_c)(lat_i - lat_c)}{\sum_i w_i} \tag{2}$$

The orientation angle of the front, θ, is obtained from the principal axis of this covariance matrix:

$$\theta = \frac{1}{2} tan^{-1}(\frac{2cov}{var_{lon} - var_{lat}}) \quad (3)$$

and the corresponding eigenvalues, representing variance along the major and minor axes, are:

$$\lambda_{1,2} = \frac{1}{2}\left[(var_{lon} + var_{lat}) \pm \sqrt{var_{lon} - var_{lat}{}^2 + 4cov^2}\right] \quad (4)$$

The frontal length and width are then defined as twice the standard deviation along the respective principal axes:

$$\begin{aligned} L &= 2\sqrt{\lambda_1} \times S_L, \\ W &= 2\sqrt{\lambda_2} \times S_W \end{aligned} \quad (5)$$

The dynamic frontal domain is then constructed as a rectangle centered on (lon_c, lat_c), oriented at angle θ, with half-length $L/2$ and half-width $W/2$. The four corners are computed by rotating the box's local coordinate axes by θ:

$$\begin{pmatrix} lon \\ lat \end{pmatrix} = \begin{pmatrix} lon_c \\ lat_c \end{pmatrix} + \begin{pmatrix} cos\theta & -sin\theta \\ sin\theta & cos\theta \end{pmatrix} \begin{pmatrix} \pm\frac{L}{2} \\ \pm\frac{W}{2} \end{pmatrix} \quad (6)$$

For each combination of signs at the four corners, corner coordinates are clamped to remain within the analysis domain (117°–125°E, 20°–28°N) where necessary. This procedure is repeated at each analysis time to produce a time-varying, front-oriented rectangular domain, which is used to evaluate the water budget in a reference frame that moves and rotates with the frontal system.

Water budget analysis

To quantify the physical mechanisms governing precipitation changes under anthropogenic forcing, we perform a water budget analysis following the framework of Trenberth and Guillemot (1995)[59], as adapted by Wang et al. (2019)[32], partitioning atmospheric water substance into vapor and hydrometeors (suspended condensates, including cloud droplets and precipitation particles). The budget equation is:

$$\underbrace{\mathrm{P} + \frac{\partial}{\partial \mathrm{t}}(\mathrm{w_v} + \mathrm{w_h})}_{\text{TDC}} = \underbrace{-\int_0^\infty \boldsymbol{\nabla} \cdot (\rho_\mathrm{v}\mathbf{V})\mathrm{dz}}_{\text{CVF}} \underbrace{-\int_0^\infty \boldsymbol{\nabla} \cdot (\rho_\mathrm{h}\mathbf{V})\mathrm{dz}}_{\text{CHF}} + \mathrm{E} + \mathrm{R} \quad (7)$$

where P is precipitation, w_v and w_h are the column vapor and hydrometeor contents, ρ_v and ρ_h are vapor and hydrometeor density, $\boldsymbol{V}$ is horizontal wind, E is evaporation, and R is the residual

term. In the tendency (TDC) term, the total water content ($w_v + w_h$) is defined as the vertical integral of vapor plus hydrometeor density. For a fixed air column, this equation states that the convergence of vapor flux (CVF) and hydrometeor flux (CHF), together with evaporation, sources the water that either falls as precipitation (P) or is stored in the column (TDC). The CVF term is further decomposed into convergence (CONV) and advection (ADV) components:

$$\underbrace{-\int_0^\infty \boldsymbol{\nabla}\cdot(\rho_v \mathbf{V})\mathrm{d}z}_{\text{CVF}} = \underbrace{-\int_0^\infty \rho_v(\boldsymbol{\nabla}\cdot\mathbf{V})\mathrm{d}z}_{\text{CONV}} \underbrace{-\int_0^\infty (\mathbf{V}\cdot\boldsymbol{\nabla})\rho_v \mathrm{d}z}_{\text{ADV}} \qquad (8)$$

CONV can be further separated into contributions from precipitable water below 5.5 km (PW5.5) and from integrated horizontal convergence below 5.5 km (IHC5.5). All budget terms are vertically integrated from the surface to 100 hPa and then spatiotemporally averaged over periods when the frontal system significantly influences Taiwan. The analysis is conducted over two domains: (1) a fixed region encompassing Taiwan (120°–122°E, 22°–25.5°N), and (2) a dynamic domain that tracks the frontal system's position over time. MERRA-2 was excluded from the water budget analysis (Table 3–Table **7**) because it does not reproduce a coherent frontal structure (Fig. 6), so the dynamic frontal domain cannot be reliably defined, and the CE–SE budget terms would not represent the anthropogenic response of the front.

Data availability

The ERA5 reanalysis data are available from the Copernicus Climate Data Store (https://cds.climate.copernicus.eu/datasets/reanalysis-era5-pressure-levels). The CFSv2, FNL, and JRA-55 analysis/reanalysis data are available from the NCAR Research Data Archive: CFSv2 (https://gdex.ucar.edu/datasets/d094000/), FNL for the 2012 case (https://gdex.ucar.edu/datasets/d083002/), and the 2017 case (https://gdex.ucar.edu/datasets/d083003/), and JRA-55 (https://gdex.ucar.edu/datasets/d628000/). The MERRA-2 reanalysis data are available from the NASA Goddard Earth Sciences Data and Information Services Center (https://disc.gsfc.nasa.gov/datasets/M2I6NPANA_5.12.4/summary). CMIP6 historical and hist-nat simulation data are available from the Earth System Grid Federation (downloadable at https://esgf.nci.org.au/search/esgf-nci/). The Central Weather

Administration (CWA) radar reflectivity, cumulative precipitation, and surface weather map data are available from the Atmospheric Science Research and Application Databank (https://asrad.pccu.edu.tw/dbar/). The QPESUMS and NCDR datasets used in this study are not publicly available but can be requested from the CWA and the National Science and Technology Center for Disaster Reduction, respectively. Data generated in this study are available from the corresponding author upon reasonable request.

Code availability

The Cloud-Resolving Storm Simulator (CReSS) model code can be downloaded from the official CReSS GitHub Repository.

References

1. IPCC. *Climate Change 2013: The Physical Science Basis* (Cambridge Univ. Press, 2014).
2. Burke, C. & Stott, P. Impact of anthropogenic climate change on the East Asian summer monsoon. *J. Clim.* **30**, 5205–5220 (2017).
3. Xu, W., Zipser, E. J. & Liu, C. Rainfall characteristics and convective properties of Mei-yu precipitation systems over South China, Taiwan, and the South China Sea. Part I: TRMM observations. *Mon. Weather Rev.* **137**, 4261–4275 (2009).
4. Ding, Y. Summer monsoon rainfalls in China. *J. Meteorol. Soc. Jpn. Ser. II* **70**, 373–396 (1992).
5. Chen, C.-S. & Chen, Y.-L. The rainfall characteristics of Taiwan. *Mon. Weather Rev.* **131**, 1323–1341 (2003).
6. Chen, X. & Chen, Y. Development of low-level jets during TAMEX. *Mon. Weather Rev.* **123**, 1695–1719 (1995).
7. Chen, G. T., Wang, C. & Lin, D. T. Characteristics of low-level jets over northern Taiwan in Mei-yu season and their relationship to heavy rain events. *Mon. Weather Rev.* **133**, 20–43 (2005).

8. Kuo, Y. & Chen, G. T. The Taiwan Area Mesoscale Experiment (TAMEX): an overview. *Bull. Am. Meteorol. Soc.* **71**, 488–503 (1990).
9. Chen, G. T.-J. Research on the phenomena of Meiyu during the past quarter century: an overview. in *East Asian Monsoon* (ed. Chang, C.-P.) 357–403 (World Scientific, 2004).
10. Lin, Y., Chiao, S., Wang, T., Kaplan, M. L. & Weglarz, R. P. Some common ingredients for heavy orographic rainfall. *Weather Forecast.* **16**, 633–660 (2001).
11. Yeh, H. & Chen, Y. Numerical simulations of the barrier jet over northwestern Taiwan during the Mei-yu season. *Mon. Weather Rev.* **131**, 1396–1407 (2003).
12. Yin, Z., Song, X., Zhou, B., Jiang, W., Chen, H. & Wang, H. Traditional Meiyu–Baiu has been suspended by global warming. *Natl. Sci. Rev.* **11**, nwae166 (2024).
13. Ding, Y., Liang, P., Liu, Y. & Zhang, Y. Multiscale variability of Meiyu and its prediction: a new review. *J. Geophys. Res. Atmos.* **125**, e2019JD031496 (2020).
14. Sun, B. et al. How does Mei-yu precipitation respond to climate change? *Natl. Sci. Rev.* **10**, nwad246 (2023).
15. Dai, L., Cheng, T. F. & Lu, M. Anthropogenic warming disrupts intraseasonal monsoon stages and brings dry-get-wetter climate in future East Asia. *npj Clim. Atmos. Sci.* **5**, 11 (2022).
16. Zhou, Z., Xie, S. & Zhang, R. Historic Yangtze flooding of 2020 tied to extreme Indian Ocean conditions. *Proc. Natl Acad. Sci. USA* **118**, e2022255118 (2021).
17. Liu, C. et al. Extreme Mei-yu in 2020: characteristics, causes, predictability and perspectives. *Earth Sci. Rev.* **246**, 104597 (2023).
18. Trenberth, K. E., Fasullo, J. T. & Shepherd, T. G. Attribution of climate extreme events. *Nat. Clim. Change* **5**, 725–730 (2015).
19. Shepherd, T. G. A common framework for approaches to extreme event attribution. *Curr. Clim. Change Rep.* **2**, 28–38 (2016).
20. Otto, F. E. L., Boyd, E. & Jones, R. G. et al. Attribution of extreme weather events in Africa: a preliminary exploration of the science and policy implications. *Clim. Change* **132**, 531–543 (2015).
21. National Academies of Sciences, Engineering, and Medicine. *The Future of Atmospheric Chemistry Research: Remembering Yesterday, Understanding Today, Anticipating Tomorrow* (National Academies Press, 2016).

22. Stott, P. A. et al. Attribution of extreme weather and climate-related events. *Wiley Interdiscip. Rev. Clim. Change* **7**, 23–41 (2016).
23. Otto, F. E. L. Attribution of weather and climate events. *Annu. Rev. Environ. Resour.* **42**, 627–646 (2017).
24. Schär, C., Frei, C., Lüthi, D. & Davies, H. C. Surrogate climate-change scenarios for regional climate models. *Geophys. Res. Lett.* **23**, 669–672 (1996).
25. Wu, W. & Lynch, A. H. Response of the seasonal carbon cycle in high latitudes to climate anomalies. *J. Geophys. Res. Atmos.* **105**, 22897–22908 (2000).
26. Wang, C.-C., Lin, B.-X., Chen, C.-T. & Lo, S.-H. Quantifying the effects of long-term climate change on tropical cyclone rainfall using a cloud-resolving model: examples of two landfall typhoons in Taiwan. *J. Clim.* **28**, 66–85 (2015).
27. Xue, Z. & Ullrich, P. Sensitivity of the pseudo-global warming method under flood conditions: a case study from the Northeastern U.S. *EGU General Assembly Conf. Abstr.* (2022).
28. Brogli, R., Heim, C., Mensch, J., Sørland, S. L. & Schär, C. The pseudo-global-warming (PGW) approach: methodology, software package PGW4ERA5 v1.1, validation, and sensitivity analyses. *Geosci. Model Dev.* **16**, 907–926 (2023).
29. Lackmann, G. M. The south-central U.S. flood of May 2010: present and future. *J. Clim.* **26**, 4688–4709 (2013).
30. Prein, A. F. et al. A review on regional convection-permitting climate modeling: demonstrations, prospects, and challenges. *Rev. Geophys.* **53**, 323–361 (2015).
31. Li, Y. et al. High-resolution regional climate modeling and projection over western Canada using a Weather Research and Forecasting model with a pseudo-global warming approach. *Hydrol. Earth Syst. Sci.* **23**, 4635–4659 (2019).
32. Wang, C.-C. et al. How much of Typhoon Morakot's extreme rainfall is attributable to anthropogenic climate change? *Int. J. Climatol.* **39**, 3454–3464 (2019).
33. Wang, C.-C. et al. Potential impacts of future climate change on super-typhoons in the western North Pacific: cloud-resolving case studies using pseudo-global warming experiments. *Atmosphere* **15**, 1029 (2024).

34. Song, F., Zhou, T. & Qian, Y. Responses of East Asian summer monsoon to natural and anthropogenic forcings in the 17 latest CMIP5 models. *Geophys. Res. Lett.* **41**, 596–603 (2014).
35. Zhou, T., Ren, L. & Zhang, W. Anthropogenic influence on extreme Meiyu rainfall in 2020 and its future risk. *Sci. China Earth Sci.* **64**, 1633–1644 (2021).
36. Wang, C.-C., Chiou, B.-K., Chen, G. T.-J., Kuo, H.-C. & Liu, C.-H. A numerical study of back-building process in a quasi-stationary rainband with extreme rainfall over northern Taiwan during 11–12 June 2012. *Atmos. Chem. Phys.* **16**, 12359–12382 (2016).
37. Chen, Y., Chu, Y., Chen, C., Tu, C., Teng, J. & Lin, P. Analysis and simulations of a heavy rainfall event over northern Taiwan during 11–12 June 2012. *Mon. Weather Rev.* **146**, 2697–2715 (2018).
38. Ke, C. Y., Chung, K. S., Wang, T. C. C. & Liou, Y. C. Analysis of heavy rainfall and barrier-jet evolution during Mei-yu season using multiple Doppler radar retrievals: a case study on 11 June 2012. *Tellus A* **71** (2019).
39. Wang, C.-C., Li, M.-S., Chang, C.-S., Chuang, P.-Y., Chen, S.-H. & Tsuboki, K. Ensemble-based sensitivity analysis and predictability of an extreme rainfall event over northern Taiwan in the Mei-yu season: the 2 June 2017 case. *Atmos. Res.* **259**, 105684 (2021).
40. Wang, C.-C., Yeh, T.-Y., Chang, C.-S., Li, M.-S., Tsuboki, K. & Liu, C.-H. A modeling study of an extreme rainfall event along the northern coast of Taiwan on 2 June 2017. *Atmos. Chem. Phys.* **23**, 501–521 (2023).
41. Wang, A.-H., Wang, C.-C. & Chen, G. T.-J. A study on synoptic conditions leading to the extreme rainfall in Taiwan during 10–12 June 2012. *Atmosphere* **12**, 1255 (2021).
42. Trenberth, K. E., Dai, A., Rasmussen, R. M. & Parsons, D. B. The changing character of precipitation. *Bull. Am. Meteorol. Soc.* 84, 1205–1218 (2003).
43. Li, C., Zhao, T., Shi, C. et al. Evaluation of daily precipitation product in China from the CMA Global Atmospheric Interim Reanalysis. *J. Meteorol. Res.* **34**, 117–136 (2020).
44. Kim, M. & Lee, E. Validation and comparison of climate reanalysis data in the East Asian monsoon region. *Atmosphere* **13**, 1589 (2022).

45. Chen, G., Iwasaki, T., Qin, H. & Sha, W. Evaluation of the warm-season diurnal variability over East Asia in recent reanalyses JRA-55, ERA-Interim, NCEP CFSR, and NASA MERRA. *J. Clim.* **27**, 5517–5537 (2014).
46. Li, X., Qin, X., Yang, J. & Zhang, Y. Evaluation of ERA5, ERA-Interim, JRA55 and MERRA2 reanalysis precipitation datasets over the Poyang Lake Basin in China. *Int. J. Climatol.* **42**, 10435–10450 (2022).
47. O'Gorman, P. A. Precipitation extremes under climate change. *Curr. Clim. Change Rep.* **1**, 49–59 (2015).
48. Guo, Y. & Nie, H. Summertime daily precipitation statistics over East China in CFSv2. *Phys. Chem. Earth A/B/C* **115**, 102841 (2020).
49. Arshad, M., Ma, X., Yin, J., Ullah, W., Liu, M. & Ullah, I. Performance evaluation of ERA-5, JRA-55, MERRA-2, and CFS-2 reanalysis datasets over diverse climate regions of Pakistan. *Weather Clim. Extremes* **33**, 100373 (2021).
50. Eyring, V. et al. Overview of the Coupled Model Intercomparison Project Phase 6 (CMIP6) experimental design and organization. *Geosci. Model Dev.* **9**, 1937–1958 (2016).
51. Gillett, N. P. et al. The Detection and Attribution Model Intercomparison Project (DAMIP v1.0) contribution to CMIP6. *Geosci. Model Dev.* **9**, 3685–3697 (2016).
52. Eyring, V. et al. Human influence on the climate system. in *Climate Change 2021: The Physical Science Basis* (eds Intergovernmental Panel on Climate Change) 423–552 (Cambridge Univ. Press, 2021).
53. World Meteorological Organization. *Technical Regulations: Basic Documents No. 2, Volume I – General Meteorological Standards and Recommended Practices* (WMO, 2023).
54. Chang, P. et al. An operational multi-radar multi-sensor QPE system in Taiwan. *Bull. Am. Meteorol. Soc.* **102**, E555–E577 (2021).
55. Tsuboki, K. & Sakakibara, A. Large-scale parallel computing of Cloud Resolving Storm Simulator. in *High Performance Computing* (eds Zima, H. P. et al.) (Lecture Notes in Computer Science vol. 2327) (Springer, 2002).

56. Tsuboki, K. & Sakakibara, A. *Numerical Prediction of High-Impact Weather Systems: The Textbook for the Seventeenth IHP Training Course in 2007* (Hydrospheric Atmospheric Research Center, Nagoya University & UNESCO, 2007).

57. Wang, C., Kuo, H., Chen, Y., Huang, H., Chung, C. & Tsuboki, K. Effects of asymmetric latent heating on typhoon movement crossing Taiwan: the case of Morakot (2009) with extreme rainfall. *J. Atmos. Sci.* **69**, 3172–3196 (2012).

58. Bolton, D. The computation of equivalent potential temperature. Mon. Weather Rev. 108, 1046–1053 (1980).

59. Trenberth, K. E. & Guillemot, C. J. Evaluation of the global atmospheric moisture budget as seen from analyses. ***J. Clim.*** 8, 2255–2272 (1995).

60. Hersbach, H. et al. The ERA5 global reanalysis. *Q. J. R. Meteorol. Soc.* **146**, 1999–2049 (2020).

61. Saha, S. et al. The NCEP Climate Forecast System version 2. *J. Clim.* **27**, 2185–2208 (2014).

62. National Centers for Environmental Prediction. NCEP GDAS/FNL 0.25 degree global tropospheric analyses and forecast grids. *NCAR Research Data Archive* https://doi.org/10.5065/D65Q4T4Z (2015).

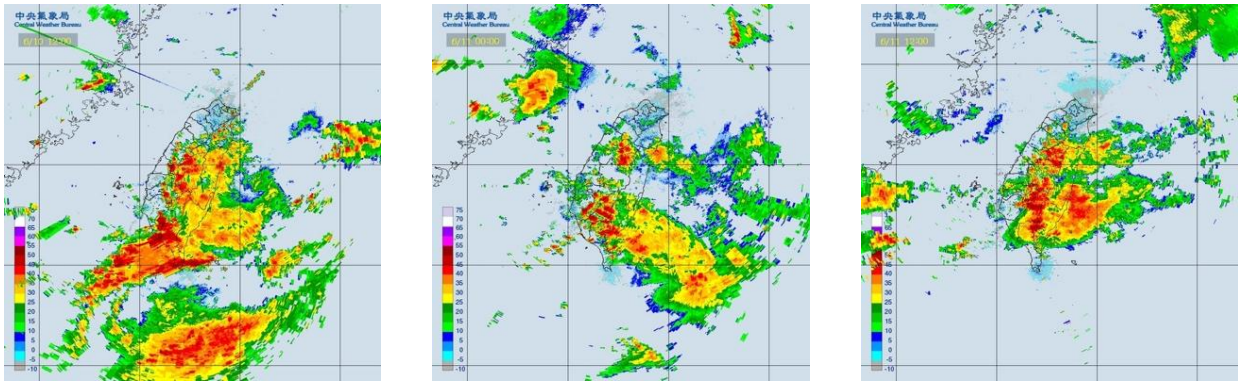
63. Kobayashi, S. et al. The JRA-55 reanalysis: general specifications and basic characteristics. *J. Meteorol. Soc. Jpn.* **93**, 5–48 (2015).

64. Gelaro, R. et al. The Modern-Era Retrospective Analysis for Research and Applications, version 2 (MERRA-2). *J. Clim.* **30**, 5419–5454 (2017).

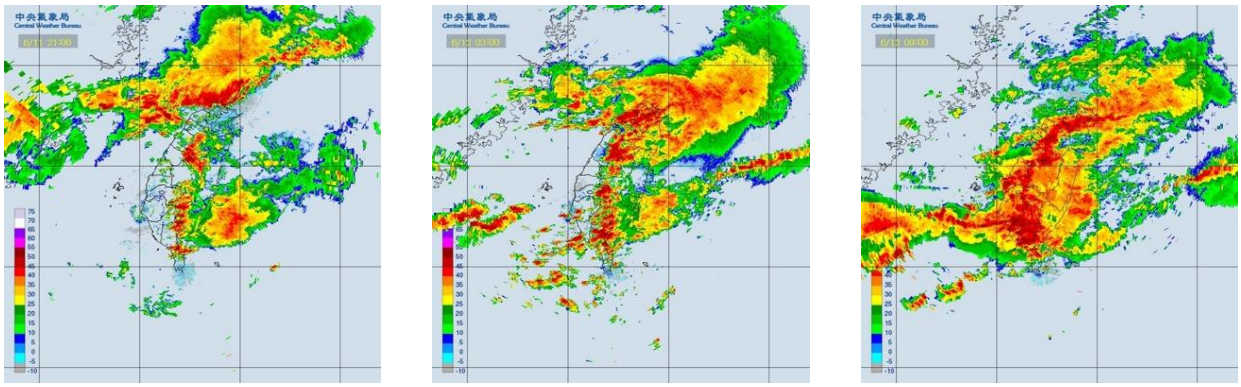
65. Huang, B. et al. Improvements of the Daily Optimum Interpolation Sea Surface Temperature (DOISST) Version 2.1. ***J. Clim.*** 34, 2923–2939 (2021).

Figures

(a) 1200 LST 10 June 2012 (b) 0000 LST 11 June 2012 (c) 1200 LST 11 June 2012



(d) 2100 LST 11 June 2012 (e) 0300 LST 12 June 2012 (f) 0900 LST 12 June 2012



(g) 1200 LST 12 June 2012 (h) 0000 LST 13 June 2012 (i) 1200 LST 13 June 2012

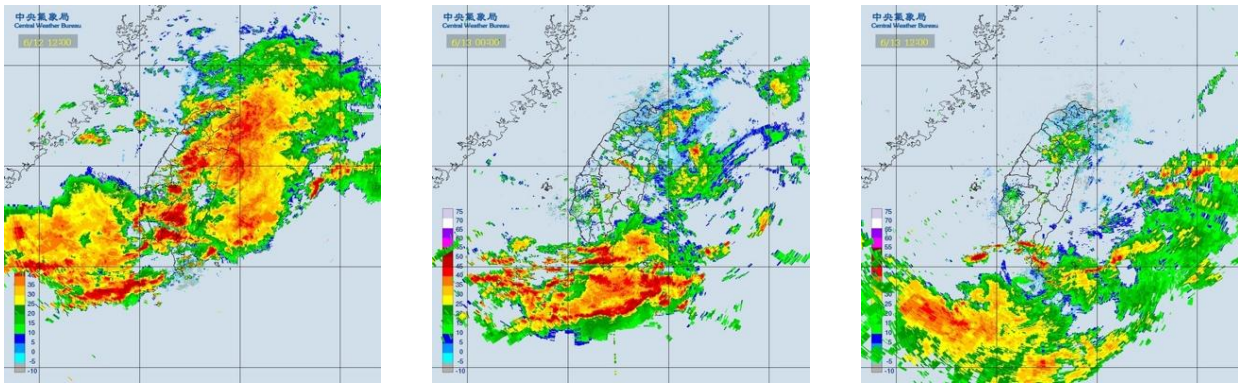
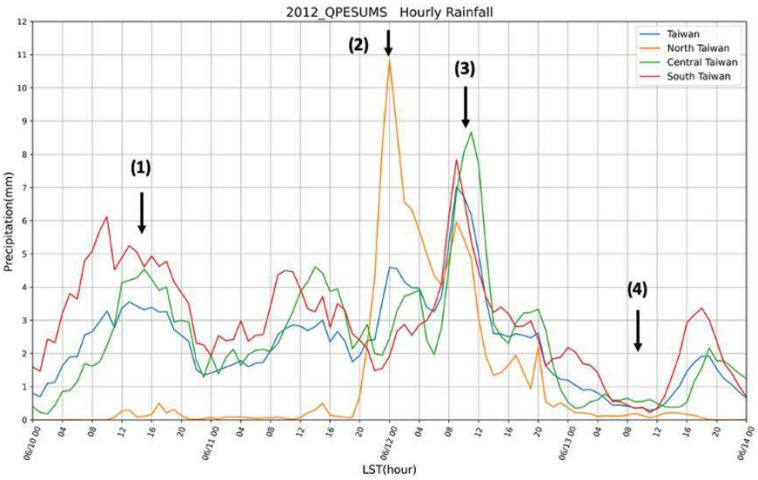


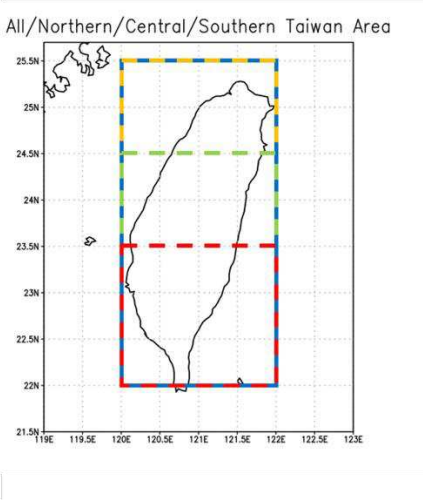
Fig. 1: Radar evolution of the 10–13 June 2012 Mei-yu event.

Composite vertical maximum indicator (VMI) radar reflectivity (dBZ) over Taiwan at (a) 1200 LST 10 June, (b) 0000 LST 11 June, (c) 1200 LST 11 June, (d) 2100 LST 11 June, (e) 0300 LST 12 June, (f) 0900 LST 12 June, (g) 1200 LST 12 June, (h) 0000 LST 13 June, and (i) 1200 LST 13 June, 2012. Source: CWA.

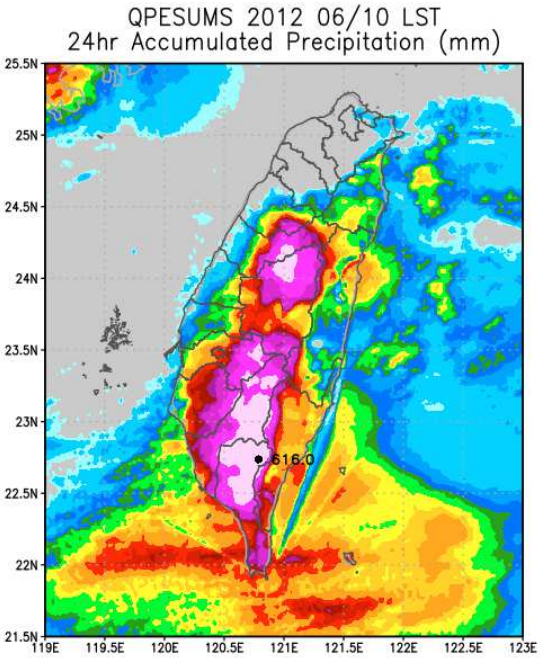
(a) 10–13 June 2012



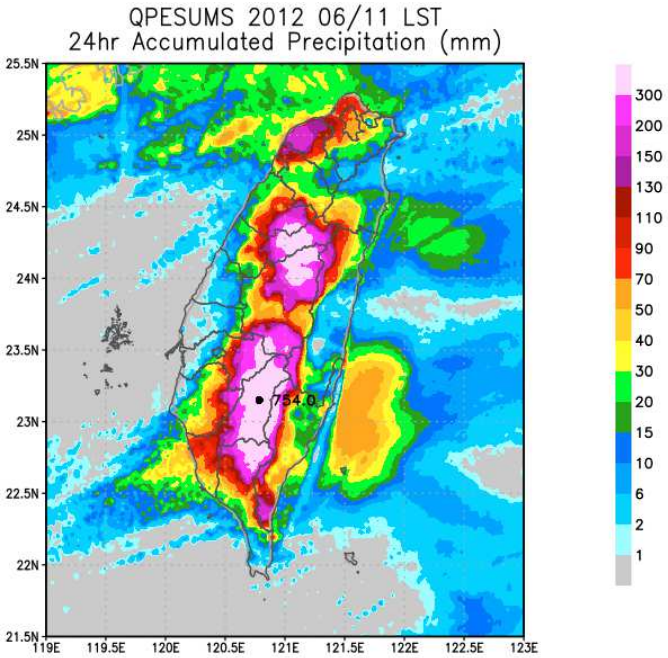
(b) 11 June 2012



(c) 10 June 2012



(d) 11 June 2012



(e) 12 June 2012

(f) 13 June 2012

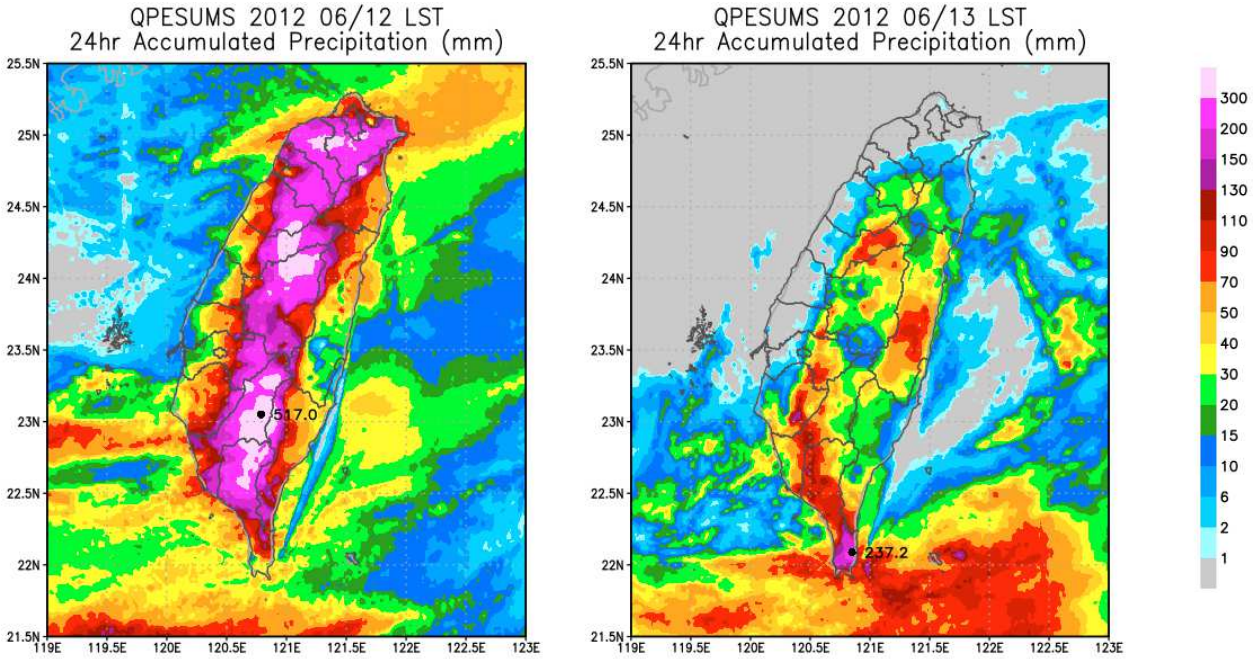
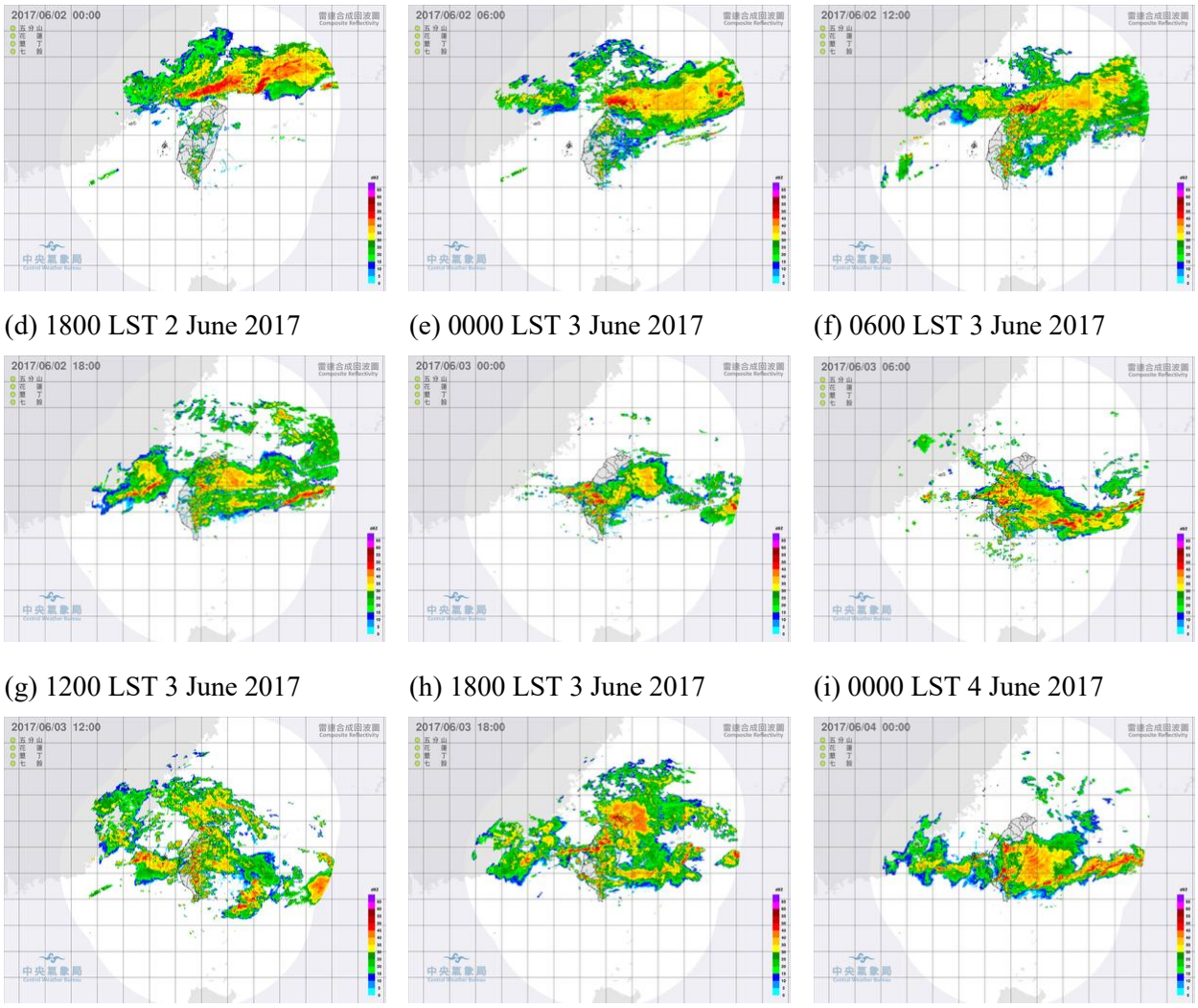


Fig. 2: Rainfall evolution during the 10–13 June 2012 Mei-yu event.

(a) Time series of domain-averaged hourly rainfall (mm) for four regions: Taiwan (blue), northern Taiwan (orange), central Taiwan (green), and southern Taiwan (red); region boundaries are shown in (b). Numbers (1–4) mark the four stages of rainfall evolution described in the text: (1) southwesterly-flow-triggered convection over southern Taiwan, (2) frontal rainband development over northern Taiwan, (3) peak island-wide rainfall from front–flow interaction, and (4) weakening. (c–f) Daily accumulated rainfall (mm) over Taiwan from 10 to 13 June 2012 (in LST), with the maximum marked by a black dot. Precipitation data are from QPESUMS.

(a) 0000 LST 2 June 2017 (b) 0600 LST 2 June 2017 (c) 1200 LST 2 June 2017



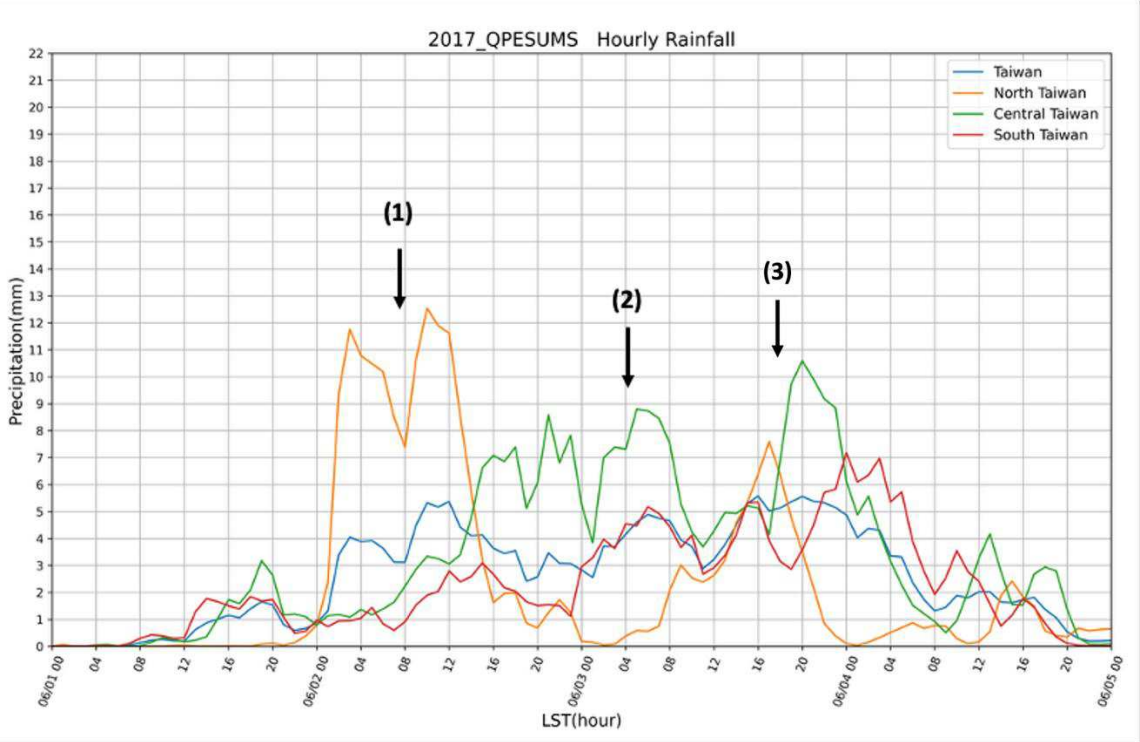
(d) 1800 LST 2 June 2017 (e) 0000 LST 3 June 2017 (f) 0600 LST 3 June 2017

(g) 1200 LST 3 June 2017 (h) 1800 LST 3 June 2017 (i) 0000 LST 4 June 2017

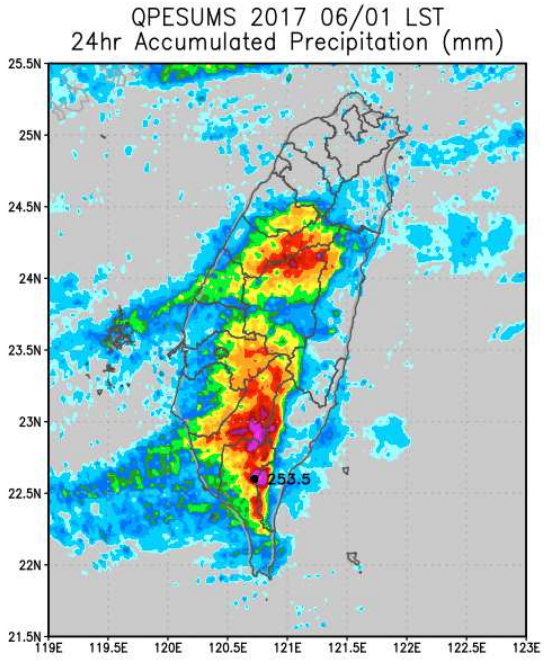
Fig. 3: Radar evolution of the 2–4 June 2017 Mei-yu event.

Composite vertical maximum indicator (VMI) radar reflectivity (dBZ) over Taiwan at (a) 0000 LST 2 June, (b) 0600 LST 2 June, (c) 1200 LST 2 June, (d) 1800 LST 2 June, (e) 0000 LST 3 June, (f) 0600 LST 3 June, (g) 1200 LST 3 June, (h) 1800 LST 3 June, and (i) 0000 LST 4 June, 2017, shown at 6-h intervals. Source: CWA.

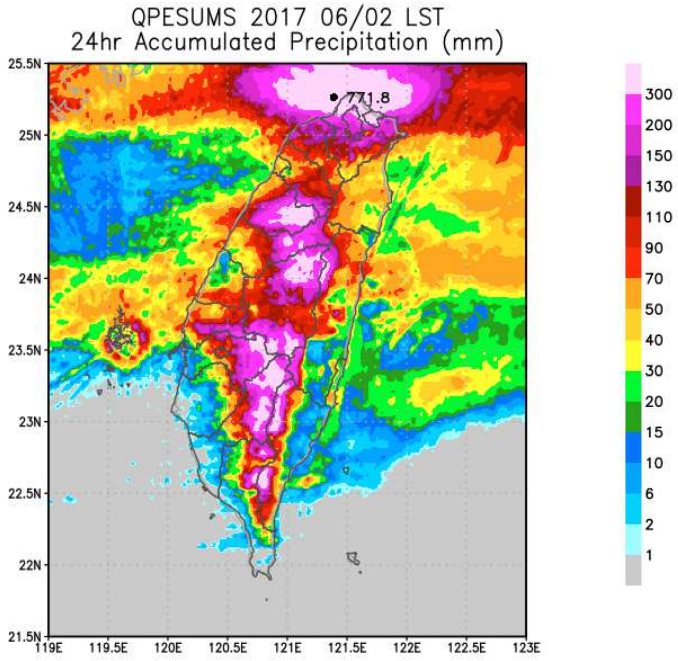
(a) 1–4 June 2017



(b) 1 June 2017



(c) 2 June 2017



(d) 3 June 2017

(e) 4 June 2017

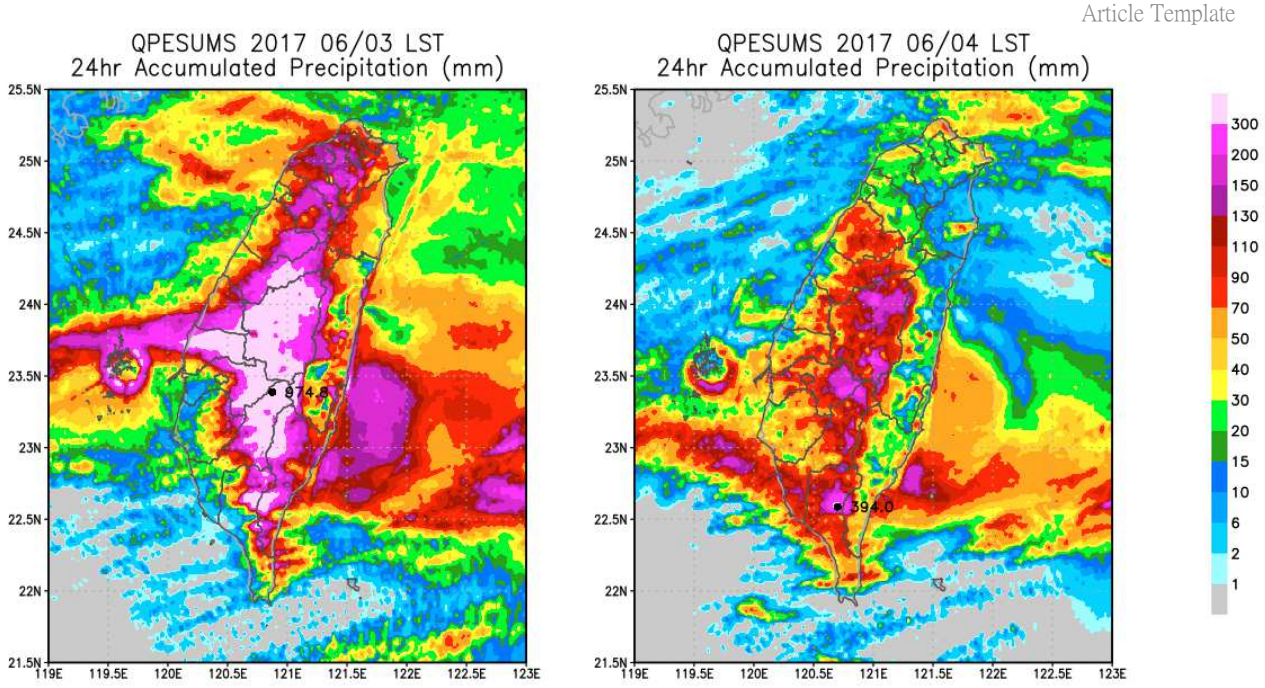
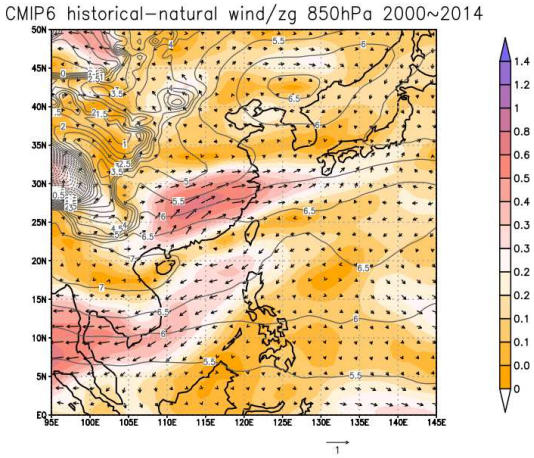


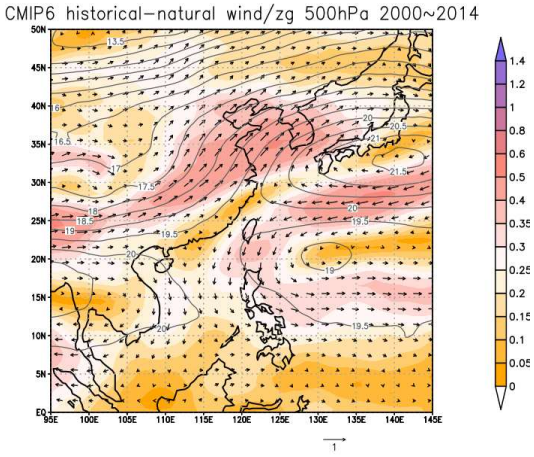
Fig. 4: Rainfall evolution during the 1–4 June 2017 Mei-yu event.

(a) Time series of domain-averaged hourly rainfall (mm) for four regions: Taiwan (blue), northern Taiwan (orange), central Taiwan (green), and southern Taiwan (red); region boundaries are shown in (Fig. 2b). Numbers (1–3) mark the stages of rainfall evolution described in the text: (1) short-duration extreme rainfall over northern Taiwan, (2) persistent heavy rainfall over central and southern Taiwan, (3) renewed rainfall across Taiwan as the front shifted northward. (c–f) Daily accumulated rainfall (mm) over Taiwan from 1 to 4 June 2017, with the daily maximum marked by a black dot. Precipitation data are from QPESUMS.

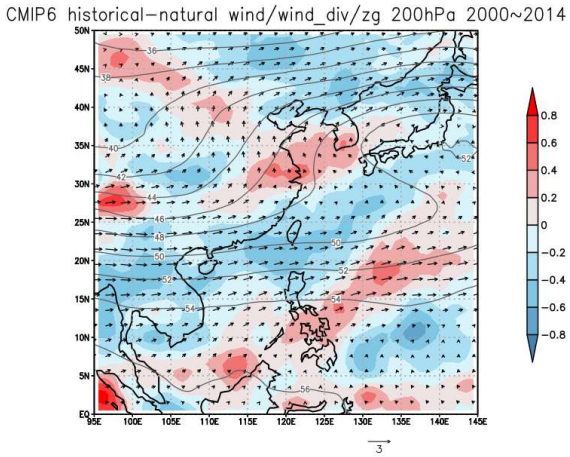
(a) wind/zg 850hPa



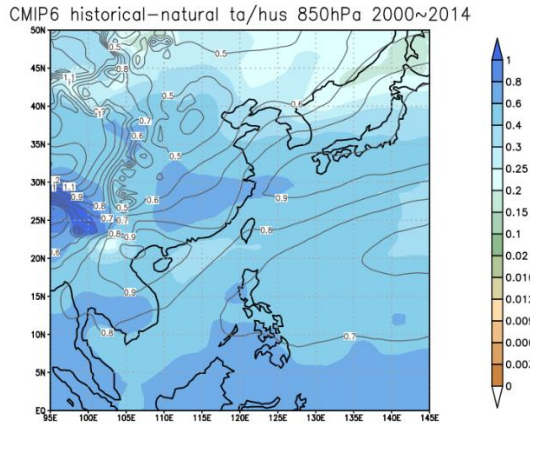
(b) wind/zg 500hPa



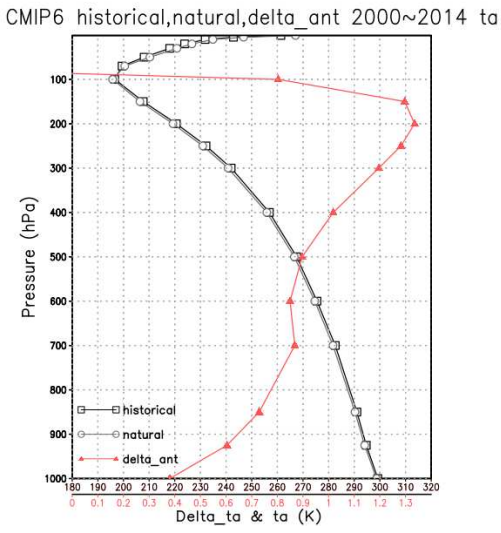
(c) wind/div/zg 200hPa



(d) ta/hus 850hPa



(e) ta – vertical profile



(f) hus – vertical profile

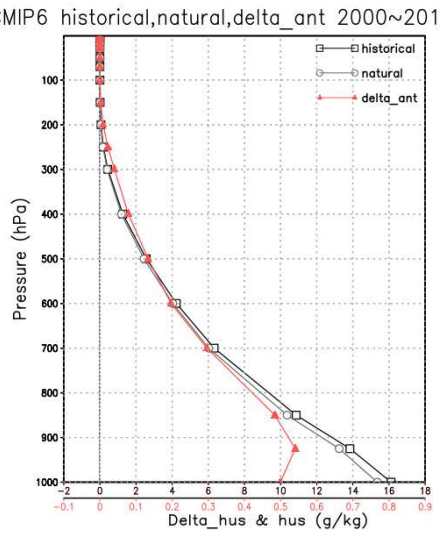


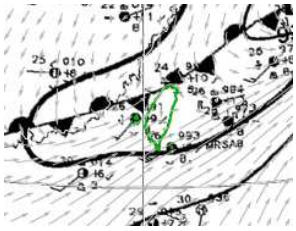
Fig. 5: Anthropogenic changes in dynamic and thermodynamic fields relevant to the Mei-yu front.

Estimated anthropogenic climate change ($\Delta ANT = \langle Historical - hist\text{-}nat \rangle_{2000\text{-}2014,\ May\text{-}June}$) in geopotential height (contours, m), horizontal wind speed (shading, m s^{-1}), and wind vectors at (a) 850 hPa and (b) 500 hPa. (c) Divergence (shading, 10^{-6} s^{-1}), geopotential height (contours, m), and wind vectors (m s^{-1}) at 200 hPa. (d) Specific humidity (shading, g kg^{-1}) and temperature (contours, K) at 850 hPa. Vertical profiles of (e) temperature and (f) specific humidity averaged over the model domain (Fig. 11) from Historical (black), hist-nat (gray), and ΔANT (red).

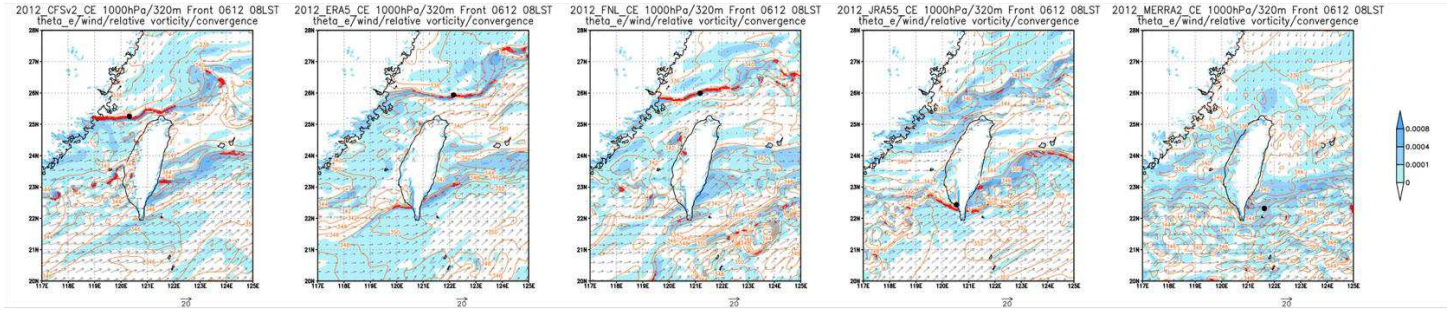
2012 case

0612 08 LST

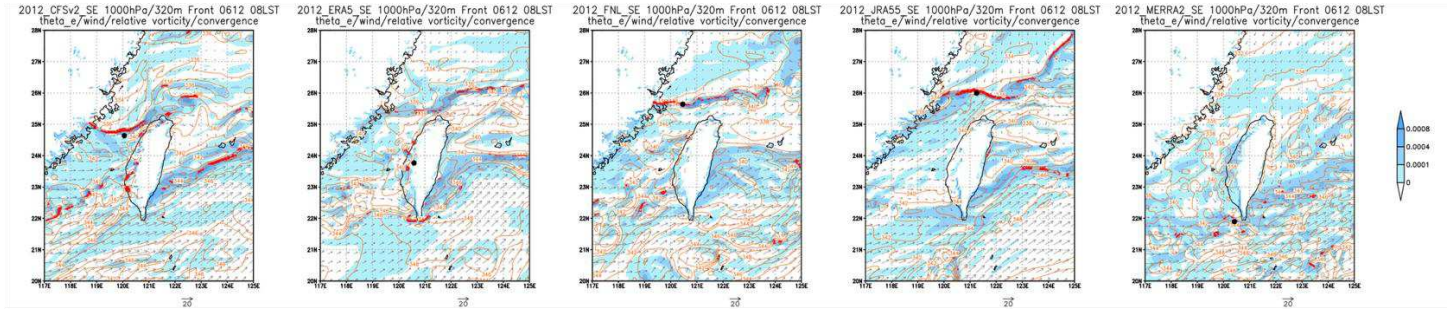
(a) CWA



(b) CE



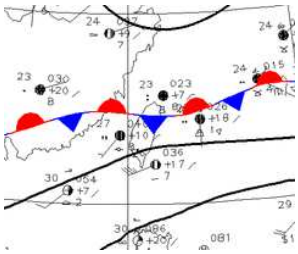
(c) SE



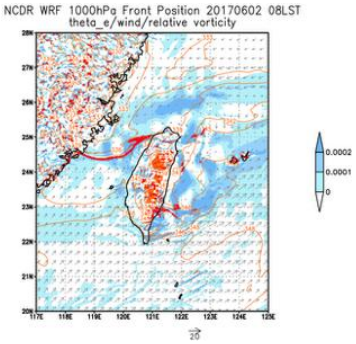
2017 case

0602 08 LST

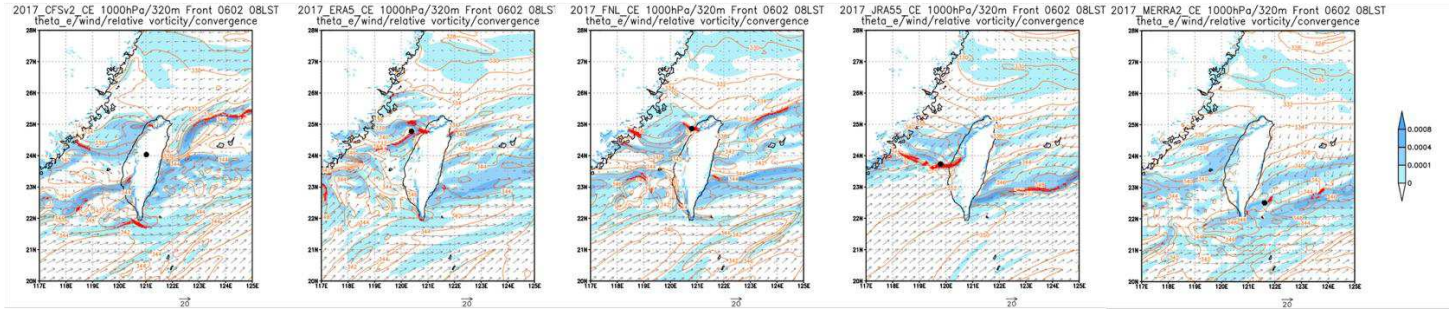
(d) CWA



(e) NCDR



(f) CE



(g) SE

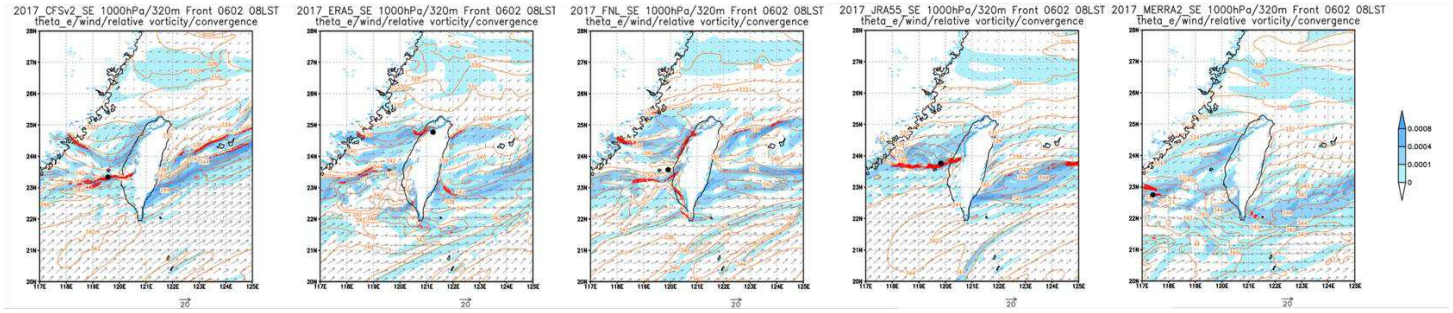
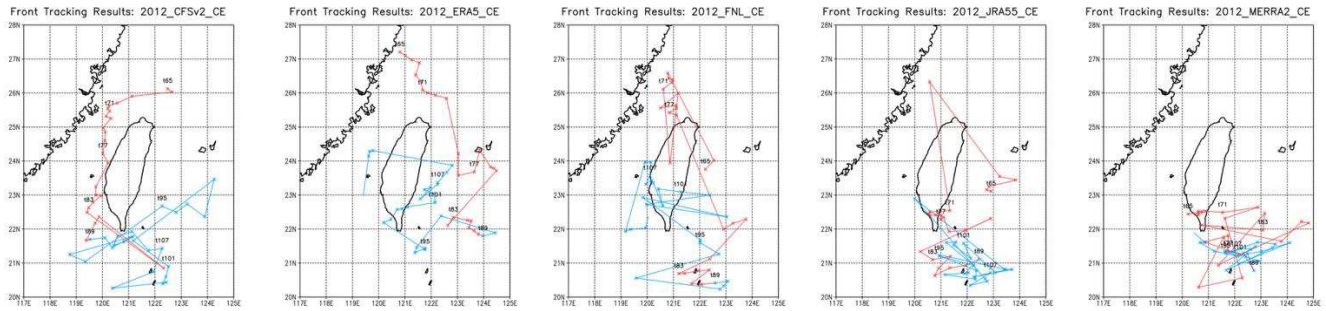


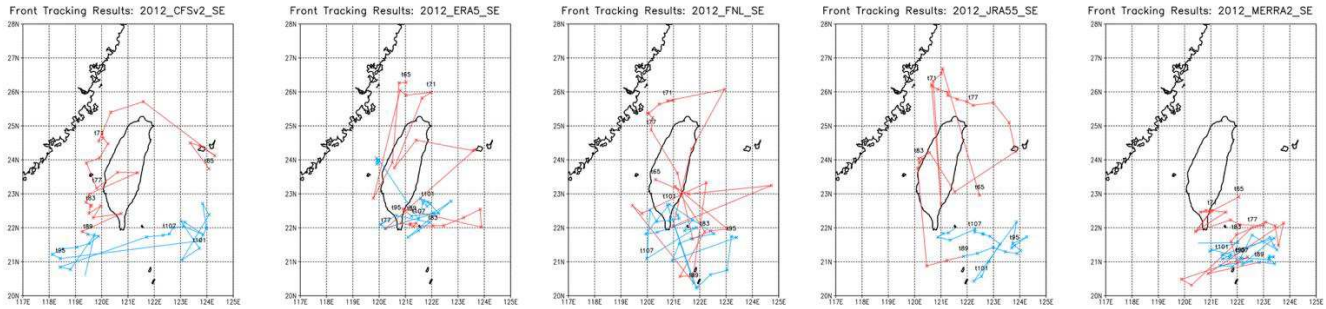
Fig. 6: Observed and simulated (CE and SE) frontal positions for the 2012 and 2017 Mei-yu events, across five sets of experiments.

Observed and simulated near-surface frontal positions at 0800 LST for (a–c) 12 June 2012 and (d–g) 2 June 2017. (a, d) CWA surface weather charts. (e) High-resolution frontal analysis from NCDR (2017 case only). (b, f) CE and (c, g) SE experiments, each showing results from five IC/BC members: CFSv2, ERA5, FNL, JRA-55, and MERRA-2 (columns 1–5). Diagnostics are based on horizontal wind (vectors, m s^{-1}), equivalent potential temperature (θ_e, contours, K), and relative vorticity (ζ, shading, s^{-1}) at 320 m (~1000 hPa). Red shading indicates frontal zones where the horizontal θ_e gradient exceeds 1×10^{-2} K m^{-1} and ζ exceeds 1×10^{-4} s^{-1}. Black dots mark frontal-center positions identified using a gradient-weighted iterative algorithm; full methodological details are provided in the Supplementary Information.

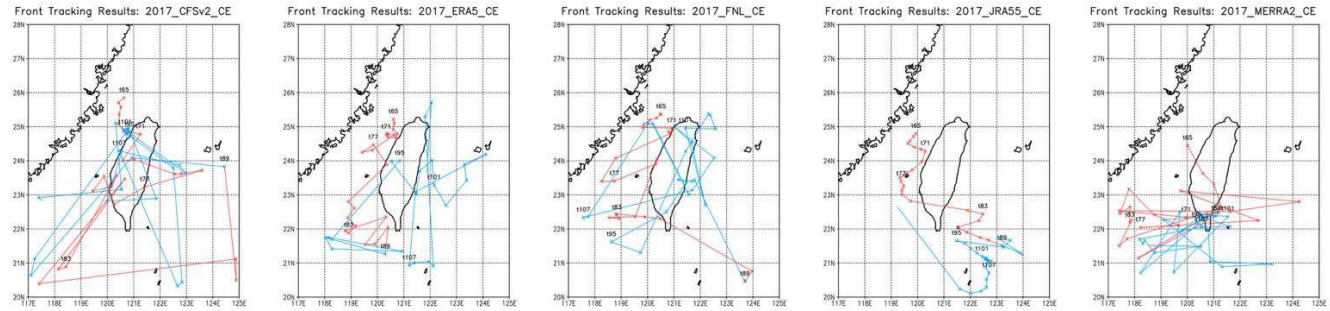
(a) 2012 CE



(b) 2012 SE



(c) 2017 CE



(d) 2017 SE

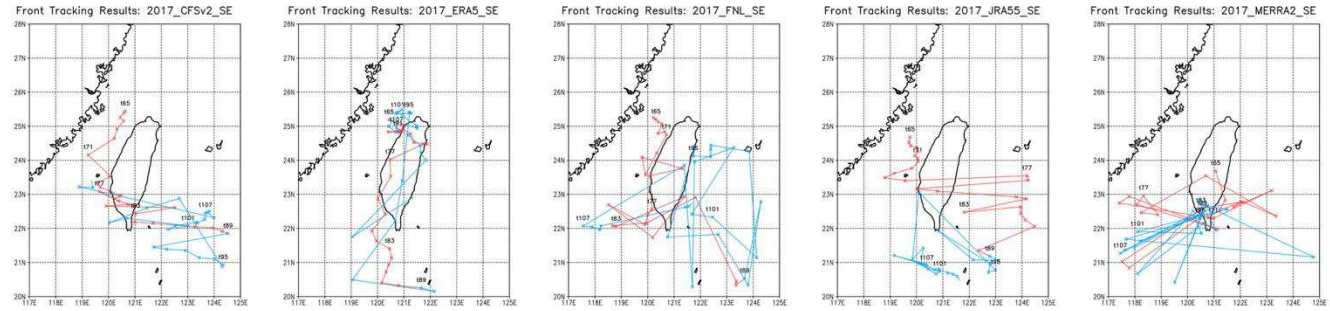
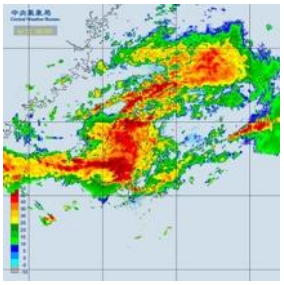


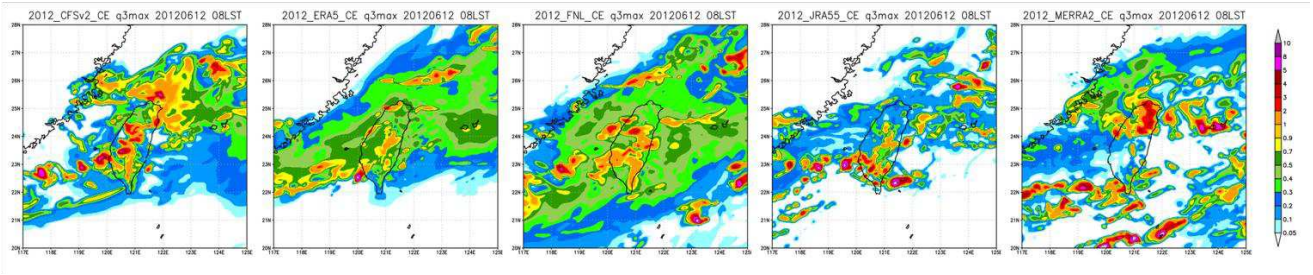
Fig. 7: Simulated (CE and SE) frontal center trajectories for the 2012 and 2017 Mei-yu events, across five sets of experiments.

Trajectories are formed by connecting the frontal-center positions in Fig. 6**:** . (a, c) CE and (b, d) SE trajectories for 12 June (red) and 13 June (blue) in the 2012 case, and for 2 June (red) and 3 June (blue) in the 2017 case.

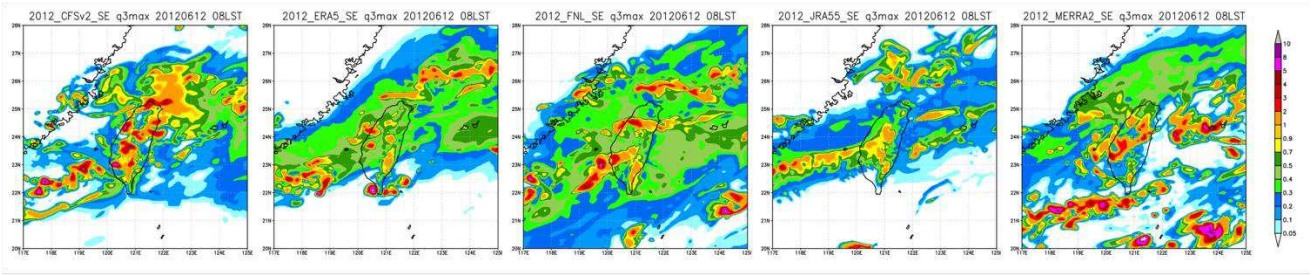
(a) 2012 CWA



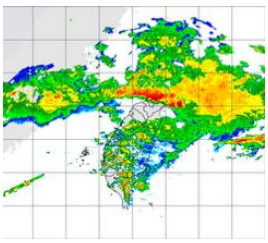
(b) 2012 CE



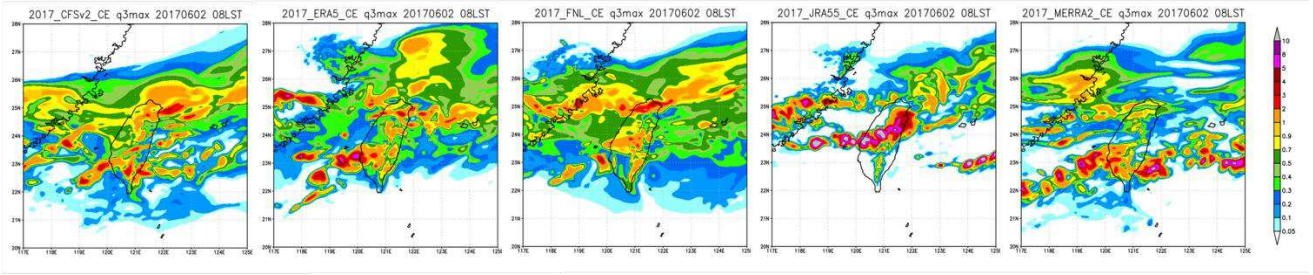
(c) 2012 SE



(d) 2017 CWA



(e) 2017 CE



(f) 2017 SE

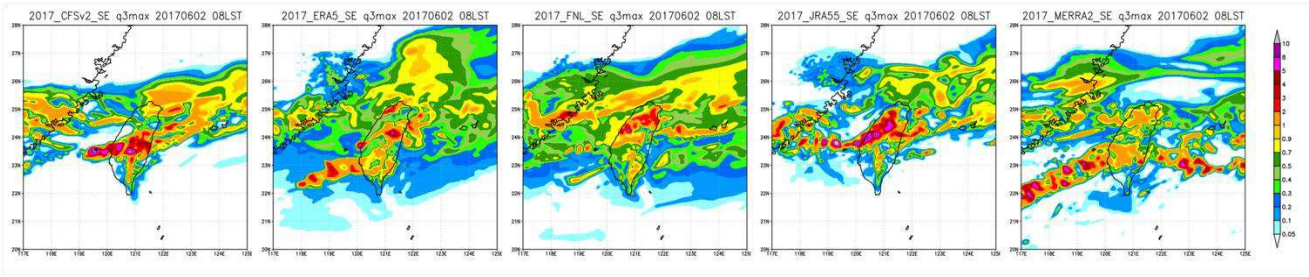
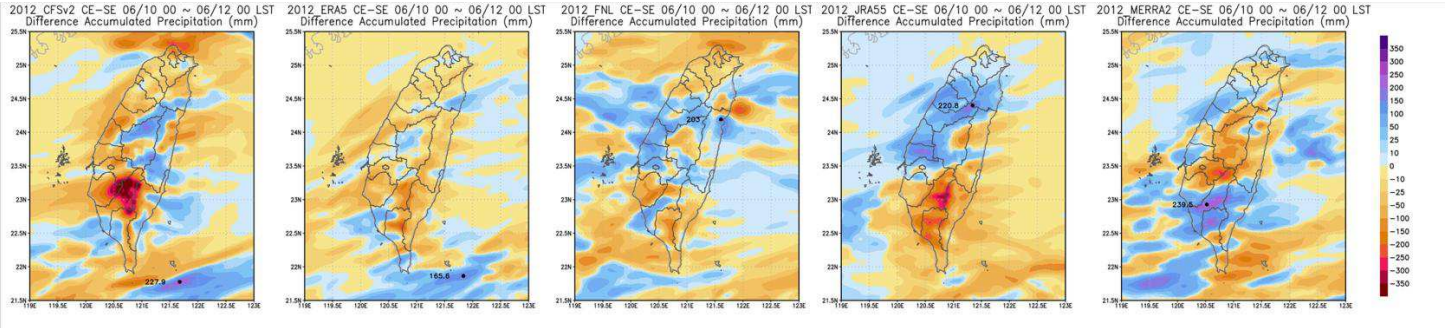


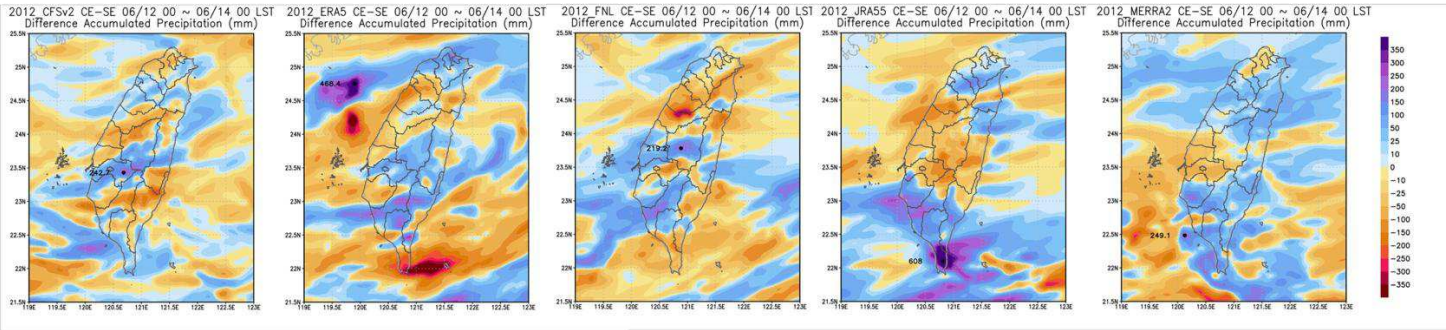
Fig. 8: Observed radar reflectivity and simulated (CE and SE) precipitation structure for the 2012 and 2017 Mei-yu events.

Precipitation structure at 0800 LST for (a–c) 12 June 2012 and (d–f) 2 June 2017. (a, d) CWA hourly radar reflectivity (dBZ). (b, e) CE and (c, f) SE experiments, showing the column-maximum mixing ratio of precipitation hydrometeors (q3max, g kg^{-1}) from five experiments: CFSv2, ERA5, FNL, JRA-55, and MERRA-2. The q3max represents the vertical maximum of total precipitation hydrometeor mixing ratio, including rain (q_r), graupel (q_g), and snow (q_s).

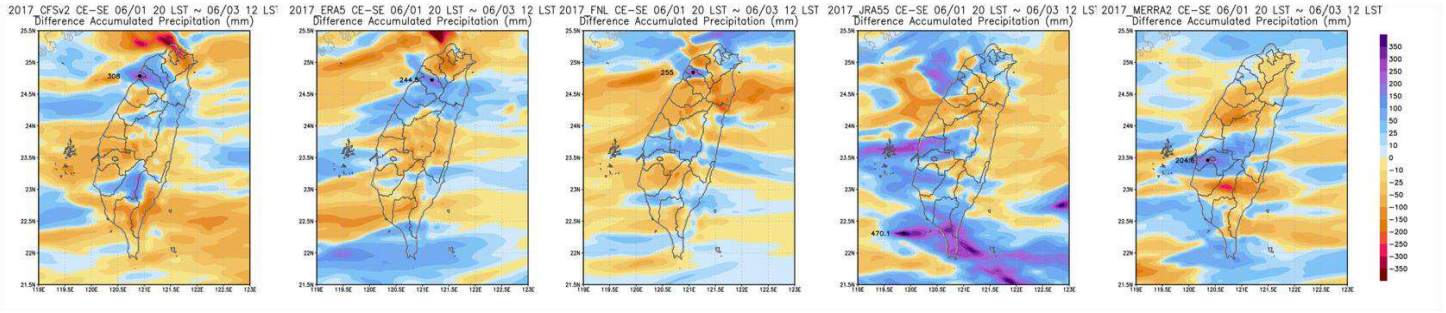
(a) 2012 case: 10–11 June



(b) 2012 case: 12–13 June



(c) 2017 case: 2000 LST 1 June – 1200 LST 3 June



(d) 2017 case: 1200 LST 3 June – 0000 LST 5 June

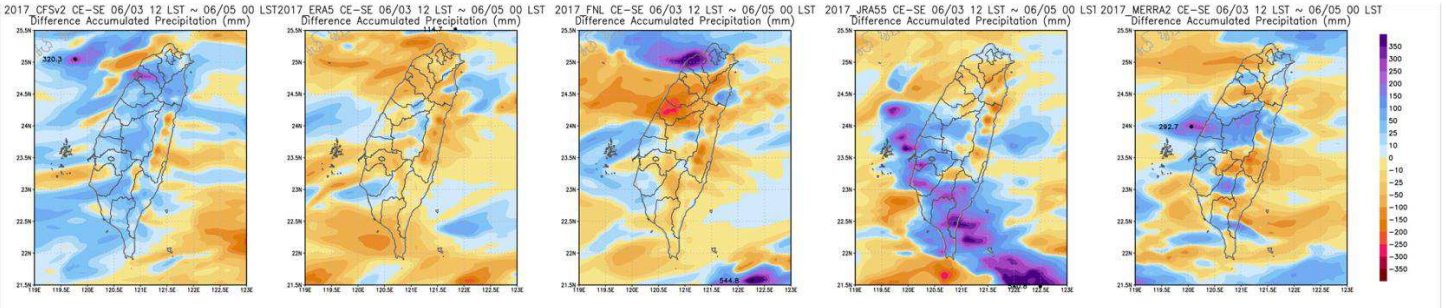
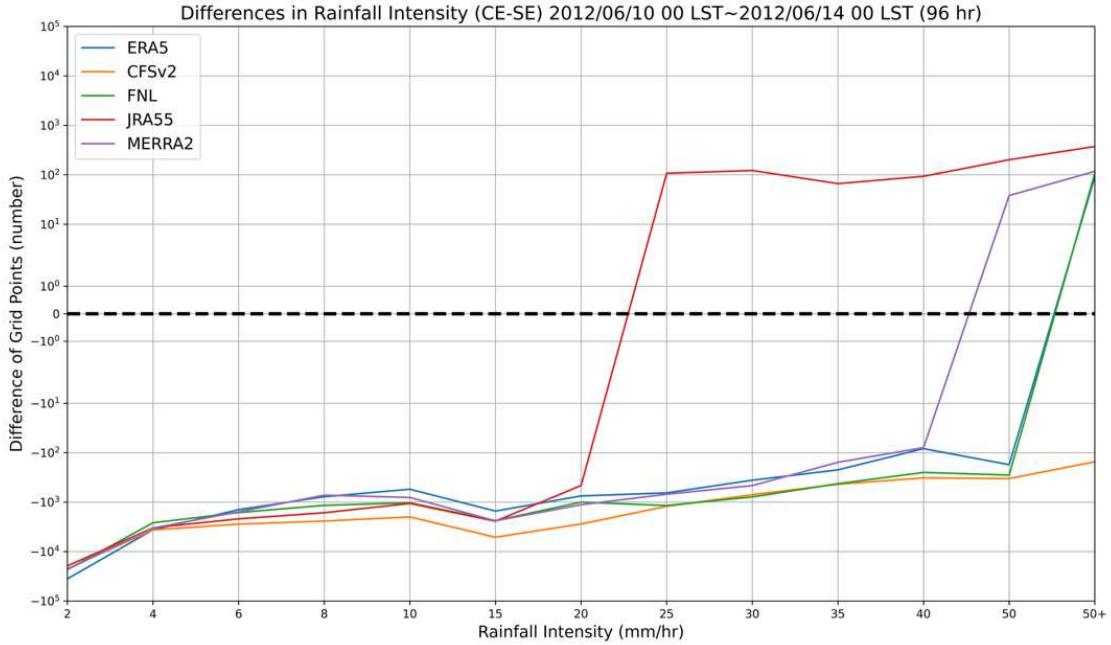


Fig. 9: Anthropogenic changes in accumulated precipitation for the 2012 and 2017 Mei-yu events.

Accumulated precipitation differences ($CE - SE$, mm) for (a) 10–11 June and (b) 12–13 June 2012, and (c) 2000 LST 1 June – 1200 LST 3 June and (d) 1200 LST 3 June – 0000 LST 5 June 2017. Results are shown for five experiments: CFSv2, ERA5, FNL, JRA-55, and MERRA-2. Shading indicates precipitation changes attributable to anthropogenic forcing, with positive (negative) values representing increased (decreased) precipitation (mm). Dots mark the location of the maximum precipitation difference within each experiment.

(a) 2012 case



(b) 2017 case

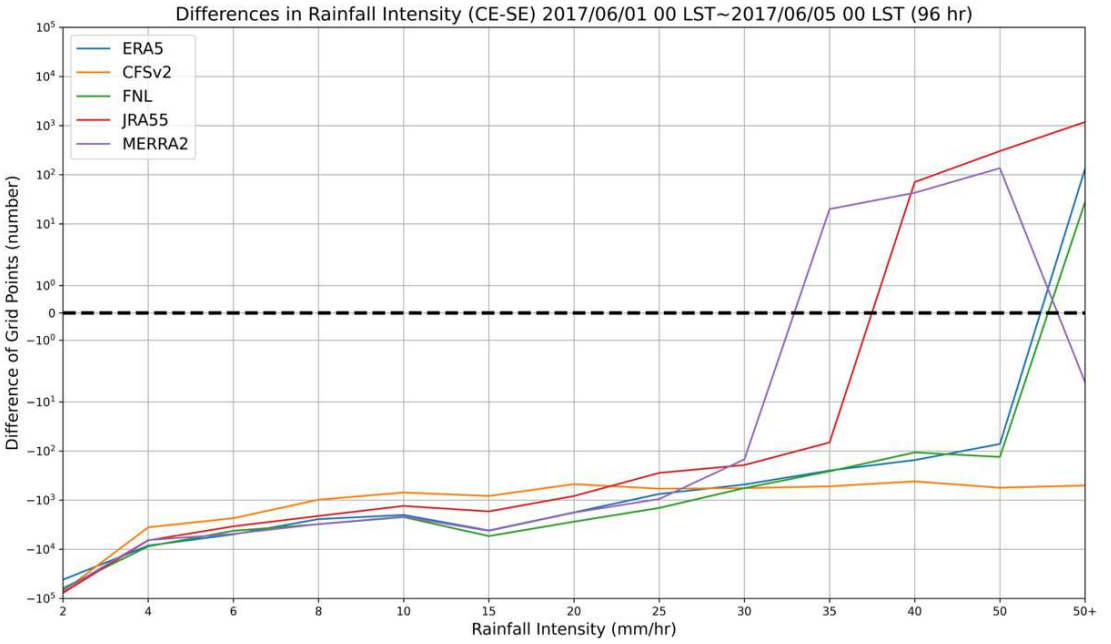


Fig. 10: Anthropogenic changes in precipitation intensity–frequency distribution over Taiwan.

Difference in grid-point counts ($CE - SE$, logarithmic scale) for each precipitation intensity bin (mm h^{-1}) from (a) 0000 LST 10 June to 0000 LST 14 June 2012, and (b) 0000 LST 1 June to 0000 LST 5 June 2017. Lines show results from ERA5 (blue), CFSv2 (orange), FNL (green), JRA-55 (red), and MERRA-2 (purple). Positive (negative) values indicate an increase (decrease) in frequency under anthropogenic forcing.

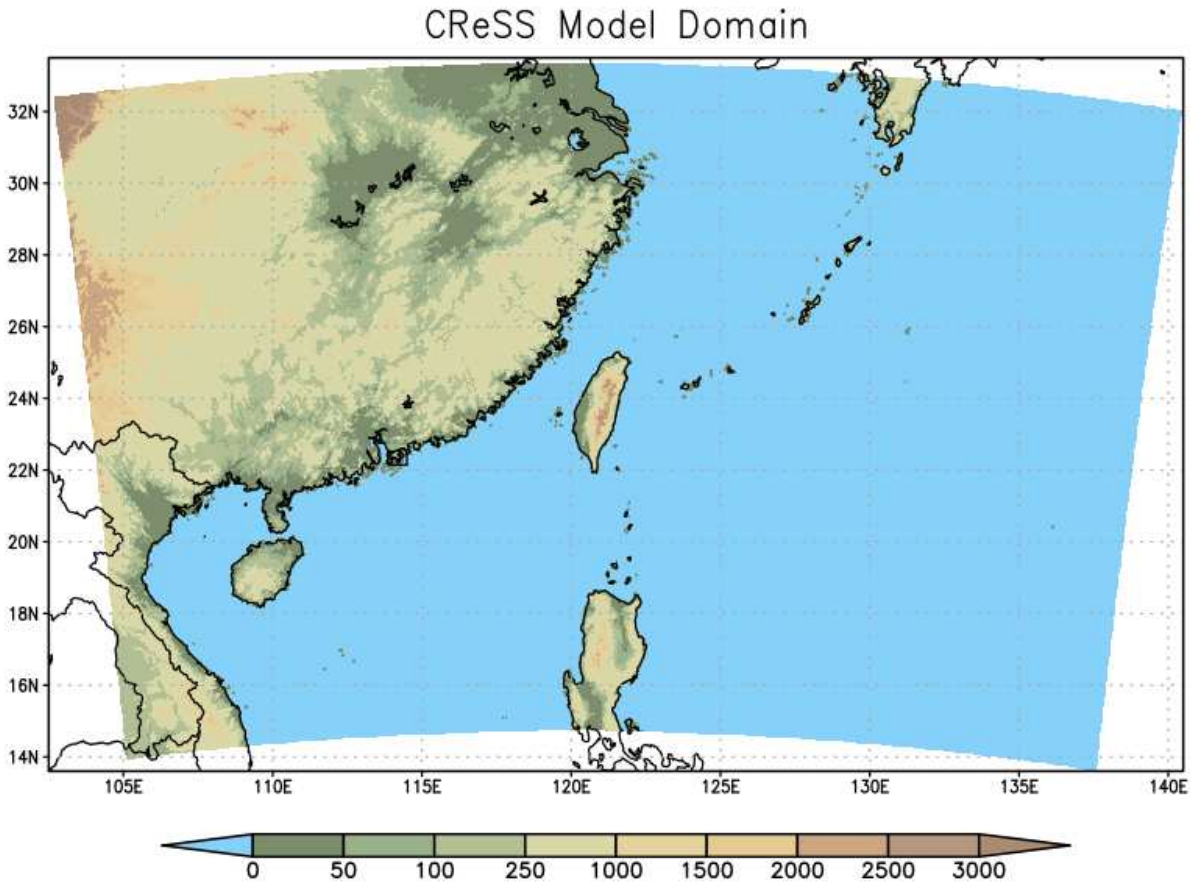


Fig. 11: Simulation domain of the Cloud-Resolving Storm Simulator (CReSS).

The shaded area (roughly 105°–140°E, 15°–35°N) indicates the model domain at 3-km horizontal resolution.

Tables

Table 1. CMIP6 models used to estimate anthropogenic climate change (ΔANT).

No.	Model	Description	Grid dimension ($Lon \times Lat$)
1	ACCESS-CM2	Commonwealth Scientific and Industrial Research Organisation, and Bureau of Meteorology (Australia)	192×144
2	ACCESS-ESM1-5	Commonwealth Scientific and Industrial Research Organisation, and Bureau of Meteorology (Australia)	192×145
3	BCC-CSM2-MR	The Beijing Climate Center Climate System Model, Beijing Climate Center, China Meteorological Administration (China)	320×160
4	CanESM5	Canadian Earth System Model version 5, Canadian Centre for Climate Modelling and Analysis (Canada)	128×64
5	CESM2	NSF–DOE–NCAR, Community Earth System Model, version 2 (USA)	288×192
6	CNRM-CM6-1	Centre National de Recherches Meteorologiques/Centre Europeen de Recherche et Formation Avancees en Calcul Scientifique (France)	256×128
7	E3SM-2-0	U.S. Department of Energy (DOE), Energy Exascale Earth System Model project (USA)	360×180
8	FGOALS-g3	LASG, Institute of Atmospheric Physics, Chinese Academy of Sciences; and CESS, Tsinghua University (China)	180×80
9	GFDL-ESM4	NOAA/Geophysical Fluid Dynamics Laboratory, Earth System Model version 4 (USA)	288×180
10	GISS-E2-1-G	NASA/Goddard Institute for Space Studies (USA)	144×90
11	HadGEM3-GC31-LL	Met Office Hadley Centre (UK)	192×144
12	IPSL-CM6A-LR	Institut Pierre-Simon Laplace (France)	144×143
13	MIROC6	Atmosphere and Ocean Research Institute (The University of Tokyo), National Institute for Environmental Studies, and Japan Agency for Marine-Earth Science and Technology (Japan)	256×128
14	MRI-ESM2-0	Meteorological Research Institute (Japan)	320×160
15	NorESM2-LM	Norwegian Climate Centre (Norway)	144×96

Models were selected based on the availability of both historical and historical-natural (hist-nat) simulations with monthly data spanning 2000–2014.

Table 2. Analysis and reanalysis datasets used to construct initial and boundary conditions for the model simulations.

Dataset	Institution	Horizontal resolution	Temporal resolution	Variables	Lower boundary condition
ERA5[60]	ECMWF	0.25° × 0.25°	6 h	*z*, *T*, *u*, *v*, RH	ERA5 SST (6 h)
CFSv2[61]	NCEP	0.5° × 0.5°	6 h	*z*, *T*, *u*, *v*, RH	NOAA OISST (daily)[65]
FNL[62]	NCEP	2012: 1° × 1° 2017: 0.25° × 0.25°	6 h	*z*, *T*, *u*, *v*, RH	FNL SST (6 h)
JRA-55[63]	JMA	1.25° × 1.25°	6 h	*z*, *T*, *u*, *v*, RH	NOAA OISST (daily)[65]
MERRA-2[64]	NASA	0.25° × 0.625°	6 h	*z*, *T*, *u*, *v*, *q*	NOAA OISST (daily)[65]

Vertical levels (25 pressure levels, 1000–20 hPa) and temporal resolution (6-hourly) are consistent across datasets, whereas horizontal resolution, variables, and lower boundary conditions vary. NOAA OISST serves as the lower boundary condition for CFSv2, JRA-55, and MERRA-2, whereas ERA5 and FNL use their own sea surface temperature fields.

z, geopotential height; *T*, temperature; *u*/*v*, zonal/meridional wind components; RH, relative humidity; *q*, specific humidity.

Table 3. Water budget analysis ((7))) in the Taiwan domain during Phase 1 (10–11 June) of the 2012 Mei-yu event.

Experiments **6/10 00LST ~ 6/12 00LST** **120°–122°E, 22°–25°N**		***P***	**TDC**	**CVF**					**CHF**	***E***	***R***	***R*/*P*** **(%)**
				Total	**CONV**			**ADV**				
					Total	**PW5.5**	**IHC5.5**					
CFSv2	CE	2.395	-0.0	2.073	1.386	52.695	3.54	0.687	-0.034	0.131	0.225	9.413
	SE	3.153	0.002	2.685	1.587	51.081	3.885	1.098	-0.011	0.135	0.346	10.985
	CE − SE	**-0.758**	**-0.002**	**-0.612**	**-0.201**	**1.614**	**-0.345**	**-0.411**	**-0.023**	**-0.004**		
	CE − SE / CE (%)	**-32%**	**-200%**	**-30%**	**-15%**	**3%**	**-10%**	**-60%**	**68%**	**-3%**		
ERA5	CE	1.028	0.055	0.804	1.816	50.29	4.256	-1.012	0.029	0.128	0.123	11.937
	SE	1.322	0.027	0.953	1.458	48.633	3.422	-0.505	0.064	0.128	0.205	15.467
	CE − SE	**-0.294**	**0.028**	**-0.149**	**0.358**	**1.657**	**0.834**	**-0.507**	**-0.035**	**0**		
	CE − SE / CE (%)	**-29%**	**51%**	**-19%**	**20%**	**3%**	**20%**	**50%**	**-121%**	**0%**		
FNL	CE	2.405	0.012	1.816	1.843	52.128	4.994	-0.027	0.137	0.107	0.358	14.881
	SE	2.576	-0.004	1.884	1.714	50.215	4.429	0.17	0.152	0.102	0.434	16.829
	CE − SE	**-0.171**	**0.016**	**-0.068**	**0.129**	**1.913**	**0.565**	**-0.197**	**-0.015**	**0.005**		
	CE − SE / CE (%)	**-7%**	**133%**	**-4%**	**7%**	**4%**	**11%**	**730%**	**-11%**	**5%**		
JRA-55	CE	0.88	0.147	0.878	1.51	51.093	3.829	-0.632	-0.0	0.104	0.045	5.14
	SE	1.164	0.056	1.028	1.466	49.4	3.539	-0.438	-0.015	0.109	0.099	8.484
	CE − SE	**-0.284**	**0.091**	**-0.15**	**0.044**	**1.693**	**0.29**	**-0.194**	**0.015**	**-0.005**		
	CE − SE / CE (%)	**-32%**	**62%**	**-17%**	**3%**	**3%**	**8%**	**31%**	**1500%**	**-5%**		

Water budget terms are precipitation (*P*), tendency of total water content (TDC), convergence of vapor flux (CVF), convergence of hydrometeor flux (CHF), evaporation (*E*), and the residual (*R*), each vertically integrated from the surface to the model top over a rectangular box domain, with the specific time period and spatial extent indicated in the upper-left corner of the table. CVF is decomposed into convergence (CONV) and advection (ADV); CONV is further compared with precipitable water below 5.5 km (PW5.5) and integrated horizontal convergence below 5.5 km (IHC5.5). All terms are given in kg m^{-2} h^{-1} (equivalent to mm h^{-1}), except $PW_{5.5}$ (mm), $IHC_{5.5}$ (10^{-2} m s^{-1}), and their percentage changes (%). CE−SE represents the effect of anthropogenic forcing; key values are highlighted in red for a reduction and blue for an increase.

MERRA-2 is not shown because its simulations do not reproduce a coherent frontal structure (Fig. 6**:**), so frontal-domain budgets cannot be reliably defined or interpreted (see Methods).

Table 4. Water budget analysis in the Taiwan domain during Phase 2 (12–13 June) of the 2012 Mei-yu event.

Experiments **6/12 00LST ~ 6/14 00LST** **120°–122°E, 22°–25°N**		***P***	**TDC**	**CVF**					**CHF**	***E***	***R***	***R*/*P*** **(%)**
				Total	**CONV**			**ADV**				
					Total	**PW5.5**	**IHC5.5**					
CFSv2	CE	2.635	-0.463	1.595	0.906	46.302	1.962	0.689	0.083	0.162	0.332	12.619
	SE	2.612	-0.477	1.601	0.798	45.291	2.392	0.803	0.057	0.15	0.328	12.549
	CE − SE	**0.023**	**0.014**	**-0.006**	**0.108**	**1.011**	**-0.43**	**-0.114**	**0.026**	**0.012**		
	CE − SE / CE (%)	**1%**	**-3%**	**0%**	**12%**	**2%**	**-22%**	**-17%**	**31%**	**7%**		
ERA5	CE	2.114	-0.08	1.626	1.935	51.535	3.78	-0.309	0.034	0.099	0.274	12.981
	SE	2.316	-0.096	1.706	1.999	48.848	4.388	-0.293	0.092	0.096	0.325	14.045
	CE − SE	**-0.202**	**0.016**	**-0.08**	**-0.064**	**2.687**	**-0.608**	**-0.016**	**-0.058**	**0.003**		
	CE − SE / CE (%)	**-10%**	**-20%**	**-5%**	**-3%**	**5%**	**-16%**	**5%**	**-171%**	**3%**		
FNL	CE	2.313	-0.161	1.642	1.391	49.934	3.284	0.251	0.008	0.084	0.417	18.031
	SE	2.463	-0.245	1.635	1.051	47.052	2.419	0.583	-0.017	0.09	0.51	20.706
	CE − SE	**-0.15**	**0.084**	**0.007**	**0.34**	**2.882**	**0.865**	**-0.332**	**0.025**	**-0.006**		
	CE − SE / CE (%)	**-6%**	**-52%**	**0%**	**24%**	**6%**	**26%**	**-132%**	**313%**	**-7%**		
JRA-55	CE	1.828	-0.249	1.316	1.364	48.715	2.855	-0.048	-0.014	0.112	0.165	9.037
	SE	1.433	-0.291	0.896	1.062	45.503	2.603	-0.116	-0.007	0.134	0.119	8.286
	CE − SE	**0.395**	**0.042**	**0.42**	**0.302**	**3.212**	**0.252**	**0.068**	**-0.007**	**-0.022**		
	CE − SE / CE (%)	**22%**	**-17%**	**32%**	**22%**	**7%**	**9%**	**-142%**	**50%**	**-20%**		

Terms and units are as defined in Table 3. Red and blue values indicate anthropogenic reduction and increase, respectively (CE−SE).

Table 5. Water budget analysis in the dynamic frontal domain for the 12 June 2012 Mei-yu event.

Experiments 6/12 00LST ~ 6/13 00LST (24-hr)		***P***	**TDC**	**CVF**					**CHF**	***E***	***R***	***R*/*P*** (%)
				Total	**CONV**			**ADV**				
					Total	**PW5.5**	**IHC5.5**					
CFSv2	CE	7.929	0.133	7.281	7.709	58.425	13.994	-0.428	-0.515	0.256	1.04	13.122
	SE	7.35	-0.134	6.094	6.561	55.592	12.731	-0.467	-0.095	0.214	1.003	13.649
	CE − SE	**0.579**	**0.267**	**1.187**	**1.148**	**2.833**	**1.263**	**0.039**	**-0.42**	**0.042**		
	CE − SE / CE (%)	**7%**	**201%**	**16%**	**15%**	**5%**	**9%**	**-9%**	**82%**	**16%**		
ERA5	CE	11.263	-0.337	11.12	12.775	59.917	19.253	-1.656	-1.663	0.142	1.328	11.788
	SE	11.111	-0.087	8.164	9.767	56.921	18.331	-1.604	-0.409	0.204	3.065	27.588
	CE − SE	**0.152**	**-0.25**	**2.956**	**3.008**	**2.996**	**0.922**	**-0.052**	**-1.254**	**-0.062**		
	CE − SE / CE (%)	**1%**	**74%**	**27%**	**24%**	**5%**	**5%**	**3%**	**75%**	**-44%**		
FNL	CE	7.576	-0.483	8.279	9.938	58.543	18.024	-1.659	-1.594	0.225	0.182	2.405
	SE	6.393	-0.109	5.106	5.926	54.441	13.155	-0.82	0.076	0.244	0.858	13.42
	CE − SE	**1.183**	**-0.374**	**3.173**	**4.012**	**4.102**	**4.869**	**-0.839**	**-1.67**	**-0.019**		
	CE − SE / CE (%)	**16%**	**77%**	**38%**	**40%**	**7%**	**27%**	**51%**	**105%**	**-8%**		
JRA-55	CE	9.938	0.447	8.83	11.153	58.889	25.562	-2.323	0.318	0.177	1.06	10.666
	SE	3.698	0.101	2.753	3.452	54.339	3.442	-0.699	-0.504	0.105	1.446	39.098
	CE − SE	**6.24**	**0.346**	**6.077**	**7.701**	**4.55**	**22.12**	**-1.624**	**0.822**	**0.072**		
	CE − SE / CE (%)	**63%**	**77%**	**69%**	**69%**	**8%**	**87%**	**70%**	**258%**	**41%**		

Terms and units are as defined in Table 3, but averaged over the dynamic frontal domain rather than the fixed Taiwan domain (see Methods for its definition and calculation). Red and blue values indicate anthropogenic reduction and increase, respectively (CE−SE).

Table 6. Water budget analysis in the Taiwan domain for the 2–3 June 2017 Mei-yu event.

Experiments **6/2 00LST ~ 6/4 00LST** **120°–122°E, 22°–25°N**		***P***	**TDC**	**CVF**					**CHF**	***E***	***R***	***R/P*** **(%)**
				Total	**CONV**			**ADV**				
					Total	**PW5.5**	**IHC5.5**					
CFSv2	CE	3.34	0.137	3.014	2.181	51.973	6.317	0.833	-0.041	0.105	0.398	11.929
	SE	3.453	0.071	3.209	2.419	50.453	5.629	0.789	-0.089	0.093	0.311	9.018
	CE − SE	**-0.113**	**0.066**	**-0.195**	**-0.238**	**1.52**	**0.688**	**0.044**	**0.048**	**0.012**		
	CE − SE / CE (%)	**-3%**	**48%**	**-6%**	**-11%**	**3%**	**11%**	**5%**	**-117%**	**11%**		
ERA5	CE	2.827	0.02	2.32	2.429	51.549	5.783	-0.109	0.046	0.096	0.385	13.625
	SE	3.339	0.055	2.751	2.284	49.346	5.351	0.467	0.091	0.103	0.449	13.439
	CE − SE	**-0.512**	**-0.035**	**-0.431**	**0.145**	**2.203**	**0.432**	**-0.576**	**-0.045**	**-0.007**		
	CE − SE / CE (%)	**-18%**	**-175%**	**-19%**	**6%**	**4%**	**7%**	**528%**	**-98%**	**-7%**		
FNL	CE	2.982	0.073	2.394	2.332	51.657	5.746	0.062	0.053	0.117	0.491	16.46
	SE	3.231	0.066	2.609	2.018	49.535	5.462	0.591	0.047	0.114	0.527	16.306
	CE − SE	**-0.249**	**0.007**	**-0.215**	**0.314**	**2.122**	**0.284**	**-0.529**	**0.006**	**0.003**		
	CE − SE / CE (%)	**-8%**	**10%**	**-9%**	**13%**	**4%**	**5%**	**-853%**	**11%**	**3%**		
JRA-55	CE	4.072	0.009	3.335	2.98	52.327	6.264	0.335	0.187	0.104	0.455	11.183
	SE	3.018	-0.009	2.519	1.919	49.549	4.489	0.601	0.029	0.093	0.368	12.18
	CE − SE	**1.054**	**0.018**	**0.816**	**1.061**	**2.778**	**1.775**	**-0.266**	**0.158**	**0.011**		
	CE − SE / CE (%)	**26%**	**200%**	**24%**	**36%**	**5%**	**28%**	**-79%**	**84%**	**11%**		

Terms and units are as defined in Table 3. Red and blue values indicate anthropogenic reduction and increase, respectively (CE−SE).

Table 7. Water budget analysis in the dynamic frontal domain for the 2–3 June 2017 Mei-yu event.

Experiments 6/2 00LST ~ 6/4 00LST		***P***	**TDC**	**CVF**					**CHF**	***E***	***R***	***R*/*P*** (%)
				Total	**CONV**			**ADV**				
					Total	**PW5.5**	**IHC5.5**					
CFSv2	CE	3.681	-0.184	3.043	3.751	57.87	3.517	-0.708	-0.724	0.049	1.129	30.665
	SE	8.376	-0.203	10.398	11.741	58.34	15.136	-1.343	-2.142	0.099	-0.182	-2.171
	CE − SE	**-4.695**	**0.019**	**-7.355**	**-7.99**	**-0.47**	**-11.619**	**0.635**	**1.418**	**-0.05**		
	CE − SE / CE (%)	**-128%**	**-10%**	**-242%**	**-213%**	**-1%**	**-330%**	**-90%**	**-196%**	**-102%**		
ERA5	CE	3.595	-0.288	4.051	5.222	57.105	4.348	-1.171	-1.119	0.08	0.295	8.208
	SE	6.01	-0.246	5.364	4.545	52.922	2.702	0.819	-0.458	0.095	0.762	12.686
	CE − SE	**-2.415**	**-0.042**	**-1.313**	**0.677**	**4.183**	**1.646**	**-1.99**	**-0.661**	**-0.015**		
	CE − SE / CE (%)	**-67%**	**15%**	**-32%**	**13%**	**7%**	**38%**	**170%**	**59%**	**-19%**		
FNL	CE	4.138	-0.253	3.632	4.228	55.979	7.283	-0.596	-0.423	0.098	0.578	13.962
	SE	2.503	-0.172	2.442	2.29	54.143	2.114	0.152	-0.448	0.12	0.218	8.695
	CE − SE	**1.635**	**-0.081**	**1.19**	**1.938**	**1.836**	**5.169**	**-0.748**	**0.025**	**-0.022**		
	CE − SE / CE (%)	**40%**	**32%**	**33%**	**46%**	**3%**	**71%**	**126%**	**-6%**	**-22%**		
JRA-55	CE	15.669	-0.335	23.427	27.461	62.807	36.78	-4.034	-9.091	0.184	0.813	5.19
	SE	7.191	-0.033	10.292	10.924	58.512	10.463	-0.632	-2.785	0.109	-0.457	-6.358
	CE − SE	**8.478**	**-0.302**	**13.135**	**16.537**	**4.295**	**26.317**	**-3.402**	**-6.306**	**0.075**		
	CE − SE / CE (%)	**54%**	**90%**	**56%**	**60%**	**7%**	**72%**	**84%**	**69%**	**41%**		

Terms and units are as defined in Table 3, but averaged over the dynamic frontal domain rather than the fixed Taiwan domain (see Methods for its definition and calculation). Red and blue values indicate anthropogenic reduction and increase, respectively (CE−SE).

Acknowledgments

This work is supported by the National Science and Technology Council of Taiwan (Grants NSTC 114-2111-M-003-004, NSTC 114-2625-M-003-004, NSTC 115-2111-M-003-004, NSTC 115-2625-M-003-002).

Author information

Authors and Affiliations

Department of Earth Sciences, National Taiwan Normal University, Taipei City 116059, Taiwan (R.O.C.)

Chung-Chieh Wang, Fang-Yu Su, Kai-En Chuang & Li-Shan Tseng

Contributions

C.C.W. and L.S.T. conceptualized and designed the experiments. F.Y.S. performed the simulations, analyzed the data, created the figures, and wrote the Chinese manuscript draft. K.E.C. modified the analyses and figures. K.E.C., L.S.T., and C.C.W. wrote the English manuscript draft. All authors contributed ideas, interpreted the results, and revised the manuscript. All authors reviewed and approved the final manuscript.

Corresponding author

Correspondence to Li-Shan Tseng

Ethics declarations

The authors declare no competing interests.

Additional information

Publisher's note Springer Nature remains neutral with regard to jurisdictional claims in published maps and institutional affiliations.

Supplementary Information (submitted as a separate file)

Rights and permissions

Open Access This article is licensed under a Creative Commons Attribution 4.0 International License, which permits use, sharing, adaptation, distribution and reproduction in any medium or format, as long as you give appropriate credit to the original author(s) and the source, provide a link to the Creative Commons licence, and indicate if changes were made. The images or other third party material in this article are included in the article's Creative Commons licence, unless indicated otherwise in a credit line to the material. If material is not included in the article's Creative Commons licence and your intended use is not permitted by statutory regulation or exceeds the permitted use, you will need to obtain permission directly from the copyright holder. To view a copy of this licence, visit http://creativecommons.org/licenses/by/4.0/.